

Precision Constraint of Deformable Bodies for Medical Imaging Applications

by

Rachel Dias Carlson

Sc.B. Mechanical Engineering
Massachusetts Institute of Technology, 2014

Submitted to the Department of Mechanical Engineering
in Partial Fulfillment of the Requirements for the Degree of
Master of Science in Mechanical Engineering

at the

Massachusetts Institute of Technology

January 2016

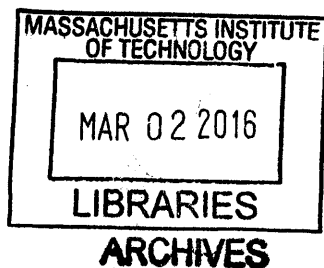
[February 2016]

© 2016 Massachusetts Institute of Technology
All rights reserved.

Signature of Author..... **Signature redacted**
Department of Mechanical Engineering
January 27, 2016

Certified by..... **Signature redacted**
Martin L. Culpepper
Professor of Mechanical Engineering
Thesis Supervisor

Accepted by..... **Signature redacted**
Rohan Abeyaratne
Professor of Mechanical Engineering
Graduate Officer



This page intentionally left blank

Precision Constraint of Deformable Bodies for Medical Imaging Applications

by

Rachel Dias Carlson

Submitted to the Department of Mechanical Engineering
on January 27, 2016 in Partial Fulfillment of the
Requirements for the Degree of Master of Science in
Mechanical Engineering

ABSTRACT

The purpose of this work is to learn how the performance of a constraint system that interfaces with nonlinear elastic materials such as biological tissue can be predicted by a model. The direct application of this work is the determination of the feasibility of restraining awake and anesthetized mice skulls to sub-micron levels of movement for biological imaging applications without direct attachment to the skull. A device capable of restricting mouse skull movement to less than a micron in every direction without requiring the rigid attachment of a fixture to the skull would enable studies of bone marrow activity that are not currently possible. No existing work has attempted to determine the performance limits of a constraint system interfacing with nonlinear elastic material. This thesis introduces a model for determining the constraint system performance, and demonstrates how material properties may be tested to determine their relative significance and inclusion in the system model. The theoretical model is applied to the case of an awake mouse to demonstrate that a tissue-interfacing constraint system can only limit movement to hundreds of microns and is not capable of achieving the desired submicron level performance. For the case of an anesthetized mouse, the designed device is tested and achieves the desired sub-micron performance in all three axes for improved imaging capabilities in anesthetized mice.

Thesis Supervisor: Martin L. Culpepper
Title: Professor of Mechanical Engineering

THIS PAGE INTENTIONALLY LEFT BLANK

ACKNOWLEDGEMENTS

I would like to thank Professor Martin Culpepper, who has been my mentor for the past three years, and from whom I have learned a great deal.

Thank you to Aaron Ramirez, for all of your help and lab wisdom, and to Lucy Du, for all of your contributions to this project.

I would like to thank all of our collaborators at MGH, both at the Center for Systems Biology and at the Martinos Center, who were the motivation for this project and without whom none of the testing would have been possible.

Finally, I want to thank my family and friends who have helped and supported me throughout my academic career.

This page intentionally left blank

CONTENTS

Abstract	3
Acknowledgements	5
Contents	7
Figures	10
Tables	12
1 Introduction	13
1.1 Mouse Use in Biological Research.....	15
1.1.1 Structures of Interest	16
1.1.2 Imaging Techniques	17
1.1.3 Motivation for Device from Literature.....	19
1.1.4 Potential Impact of Device on Experimental Design	20
1.2 Existing Restraint Methods and Limitations.....	20
1.2.1 Prior Art; Stereotaxic devices and Restraint Devices	20
1.2.2 Performance and Limitations of Previous Prototype	22
1.3 Requirements for Improved Restraint Device	25
1.3.1 Functional Requirements for Restraint Device	25
1.3.2 Critical properties of Laboratory Mice.....	26
1.4 Thesis Summary.....	27
2 Constraint Methods and System Modeling	29
2.1 Design Constraints	29
2.1.1 Contact Options.....	30
2.1.2 Active vs. Passive Constraint	31
2.2 System Model	33
2.3 Contact Stiffness	34
2.3.1 Hertzian Contact Stiffness Overview	34

2.3.2	FEA Model of System Stiffness.....	36
2.4	Material Properties of Mouse Tissue	39
2.4.1	Mouse Muscle Layer Properties.....	39
2.4.2	Mouse Skin Properties	40
2.4.3	Mouse Bone Properties	43
2.4.4	Summary of Material Properties	44
2.5	Force Generated by Mouse	44
3	Design of Material Testing Setup	46
3.1	Functional Requirements for Materials Testing	46
3.2	Mechanical Design of Setup	48
3.2.1	Axis Actuation Mechanisms	48
3.2.2	Sensors and Control	52
3.3	Error Model and Uncertainty	54
3.4	Functional Requirements Revisited	55
4	Experimental Design and Results.....	56
4.1	Preparation of Mice.....	56
4.2	Shear Stiffness Testing Procedure	58
4.3	Young's Modulus (Axial Stiffness) Procedure.....	59
4.4	Results.....	62
4.4.1	Shear Stiffness Testing Results	62
4.4.2	Axial Stiffness Testing Results	64
4.5	Discussion and Comparison to Published Values.....	65
5	Predicting Constraint System Performance.....	68
5.1	System Behavior	68
5.2	Dimensional Analysis	72
5.3	Calculating Maximum Allowable Contact Force	75
5.3.1	Bone Model and Failure Criteria.....	75
5.3.2	Maximum Force Calculations	76
5.4	Discussion of Expected Performance	77
5.4.1	Performance for Anesthetized Mice.....	79

6 Design of Restraint Device	80
6.1 Functional Requirements	80
6.2 Application of Kinematic Constraint Theory	81
6.2.1 Assumptions for Kinematic Constraint	81
6.2.2 Geometry of Mouse Skull	82
6.2.3 Constraint Location Selection	83
6.3 Mechanical Design.....	85
6.3.1 Use Case Considerations.....	85
6.3.2 Design Overview.....	86
7 Performance of Restraint Device.....	89
7.1 Performance Characterization Procedure	89
7.1.1 Testing Procedure.....	89
7.1.2 Experimental Setup	90
7.2 Results.....	93
7.2.1 Material Properties	93
7.2.2 Predicted Performance	93
7.2.3 Actual Performance.....	94
7.3 Discussion.....	97
8 Conclusions and Future Work.....	99
8.1 Thesis Synopsis.....	99
8.2 Future Work	100
8.2.1 Validation of Theoretical Model	100
8.2.2 Improvements to Restraint Device.....	100
8.2.3 Application of Theory to Human Restraint.....	101
References.....	102
A Appendix: Electronics.....	105
A.1 VCA Electronics	105

FIGURES

Figure 1.1: Prototype restraint device with mouse	14
Figure 1.2: Mouse movement measured during prototype testing	15
Figure 1.3: Laboratory Mouse with Skin Cleared from Imaging Area of Interest.	16
Figure 1.4: Cortical bone and bone marrow compartment with GFP+ cells.	18
Figure 1.5: Current restraint devices for brain imaging.....	21
Figure 1.6: Prototype designed by Culpepper et al.....	23
Figure 1.7: Experimental Setup (a) without and (b) with Capacitance Probes.....	23
Figure 1.8: Motion of skull in Z axis while mouse is anesthetized (a) and (b). Motion of skull while animal is waking (c) and fully awake (d).....	24
Figure 2.1: Titanium human skull pin used for positioning the head during imaging.....	30
Figure 2.2: Mouse skull and associated degrees of freedom.	33
Figure 2.3: Spring stiffness model for constraint system and mouse.	34
Figure 2.4: Diagram of Hertzian Contact.	35
Figure 2.5: Setup for FEA Simulation	36
Figure 2.6: FEA Results for Test 1 (contact and bone modeled with real world values).	37
Figure 2.7: Side view of skin and bone displacement for Test 1	38
Figure 2.8: Muscle visible in cheek area once skin is removed.....	39
Figure 2.9: Skin layers in wild type mouse.....	41
Figure 2.10: Example of stress-strain curve for nonlinear elastic materials.....	42
Figure 3.1: Modes of mouse movement in relation to contact	47
Figure 3.2: Load path from voice coil to mouse.....	49
Figure 3.3: Elements controlling travel in the y axis.	50
Figure 3.4: Schematic of load path and displacement of elements in y axis.	51
Figure 3.5: Side view of testing setup and voice coil load path	52
Figure 3.6: Voice Coil actuation with Labview control	52
Figure 3.7: Current control schematic for VCA operation.	53
Figure 3.8: Thermal regulation box surrounding the setup.....	55

Figure 4.1: (a) Setup plate being glued to mouse skull (b) Mouse fixed in setup	57
Figure 4.2: Screw and dental cement attachment	57
Figure 4.3: Instron setup schematic	61
Figure 4.4: Instron testing setup.....	61
Figure 4.5: Shear stiffness as a function of input displacement	63
Figure 4.6: Data from multiple skin trials plotted against eqn 15, $p = 35$	64
Figure 4.7: Stiffness curve for $p=25.25$, with red dot representing point around which Young's Modulus was calculated with step size of $10\mu\text{m}$	67
Figure 5.1: Spring model and force inputs for derivation of mouse position error, δ	69
Figure 5.2: Nonlinear stiffness curve.....	71
Figure 5.3: Graph of non-dimensional parameters π_3 (q) vs π_2 (\mathcal{E}) as a function of π_1 (Fratio.....	74
Figure 5.4: 3 point bending schematic	75
Figure 5.5: Mouse skull with proposed contact locations encircled and numbered	77
Figure 6.1: Areas to avoid contact on mouse skull	83
Figure 6.2: Contact locations needed to constrain all six rigid body degrees of freedom.....	84
Figure 6.3: Restraint Device	85
Figure 6.4: (a) Direction of constraint shown for each contact (b) Top view	87
Figure 6.5: (a) Side view (b) Contact locations on skull with colors corresponding to contacts .	87
Figure 7.1: Rear view of experimental setup	91
Figure 7.2: Mouse tightened in restraint device.....	92
Figure 7.3: Mouse fixed in performance characterization setup.....	92
Figure 7.4: Raw and filtered data for x displacement	94
Figure 7.5: Close up of y displacement showing respiration and heartbeats.....	95
Figure 7.6: Y displacement of skull (a) with and (b) without rear contact.....	95
Figure 7.7: Displacement in the x axis for an awake mouse	96

TABLES

Table 1: Structures of Interest for Proposed Biological Imaging Applications.....	17
Table 2: Imaging Techniques.....	18
Table 3: Restraint Device Functional Requirements.	25
Table 4: Laboratory Mice Physiological Properties	26
Table 5: Hertzian Contact Theory Applicability	35
Table 6: FEA System Stiffness Results.	38
Table 7: Classification of Tissue Layers.....	44
Table 8: Functional Requirements for Material Testing Setup.....	47
Table 9: Error Sources for Material Testing Setup.....	54
Table 10: Functional Requirements Revisited.....	55
Table 11: Shear Stiffness Values.	63
Table 12: Measured Material Properties.....	65
Table 13: Material Property Values.....	65
Table 14: Maximum Contact Force at Skull Locations	77
Table 15: Input Ranges for Performance Characterization.....	78
Table 16: Restraint Device Functional Requirements.	80
Table 17: Material Properties for Mouse used in Performance Characterization Tests.	93
Table 18: Measured Displacement of Anesthetized Mouse Skull in Restraint Device.	96
Table 19: Restraint Device Functional Requirements Revisited.	98

CHAPTER

1

INTRODUCTION

The purpose of this thesis is to learn how an object's material properties set the limits of a constraint system's ability fixation performance, characterized by the maximum movement of the object while constrained. This understanding is then applied to the specific case of restraining laboratory mice for imaging procedures. The work presented here includes: the design of a material property testing setup for mouse tissue; characterization of the material properties of mouse tissue in normal and shear directions; the development of a model for predicting the performance of a constraint system based on material properties; the design of a mouse constraint device, and the preliminary testing results of the device with a comparison to the values predicted by the model. Existing research has not explored the shear properties of mouse tissue, and no data is available for the properties of the muscle layer. The constraint devices and techniques currently available for mice have several limitations that are addressed in this thesis. The model presented in this thesis may be used to design a constraint system and describe its performance when interfacing with any nonlinear elastic material.

The direct application of this work is the restraint of laboratory mice for improved biological imaging. The ability to view micron and sub-micron scale structures with the resolution needed over extended time periods is currently limited by the movement of the mouse subject. Limiting the movement of the mouse will enable different types of experiments to be done, as structures may be examined or tracked with the accuracy necessary to make a meaningful claim.

Previously, no attempt has been made to characterize exactly what the best case performance of a restraint device is, and no device has been designed from a mechanical constraint point of view. While this thesis aims to minimize the movement of anesthetized mice, the potential application to awake mice will also be explored. This research characterizes the critical properties of mouse tissue and develops a method for characterizing the constraint system performance in order to inform the feasibility and design of a restraint device. The prototype restraint device is shown in Figure 1.1. The mouse is shown tightened into the device, with skin removed from the imaging area located at the top of the skull.

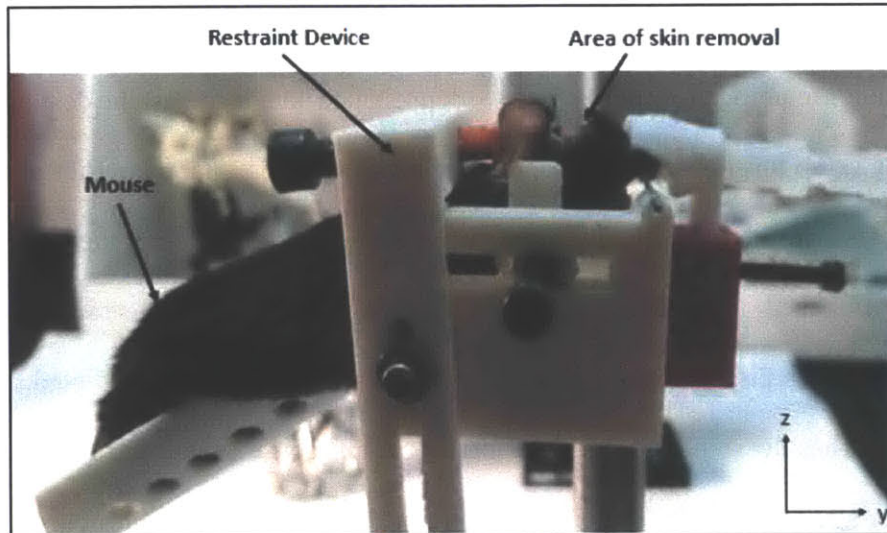


FIG 1.1: Prototype Restraint Device with Mouse

The movement of the mouse may then be measured either through post processing of any images taken or through direct measurement of conductive material attached to the skull. Figure 1.2 shows a small time frame of measured displacement data in the x axis.

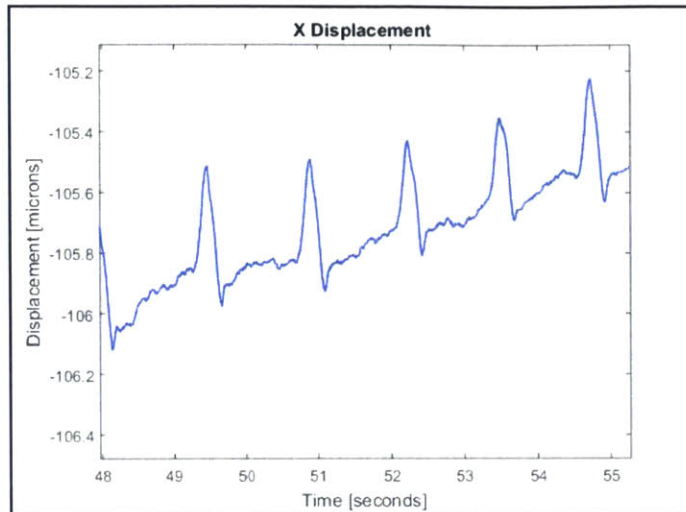


FIG 1.2: Mouse movement measured during prototype testing

This image clearly shows the displacements associated with the respiration and heartbeat of the mouse. This thesis details the development of a model to predict the performance of a constraint system and its use in the design of the restraint device, beginning with an overview of the motivation and need for such a device.

1.1 Mouse Use in Biological Research

In vivo studies of live animals result in many advancements in biomedical and clinical research. Animal models provide a platform to study therapeutic responses and the progression of disease in ways which require manipulation that cannot be performed on humans. These studies utilize imaging techniques with sub-micron resolution to characterize tissue structure and physiological activity in animal models. The mouse is the most commonly used mammalian model for laboratory research due to its genetic and physiological similarity to humans [1]. Current imaging techniques and structures of interest will be summarized so that the need and application for an improved restraint device may be better understood.

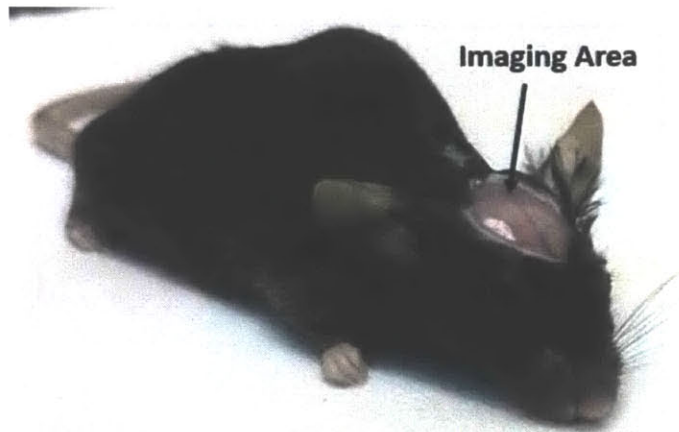


FIG 1.3: Laboratory Mouse with Skin Cleared from Imaging Area of Interest

1.1.1 Structures of Interest

While there are many potential applications with a variety of target structures, three specific applications have been identified. These applications require clear images of the behavior of small structures such as pericytes, red blood cells and dendrites. Imaging of retinal ganglion cells and microglia may be achieved with a confocal scanning laser ophthalmoscope that excites multiple fluorophores in order to track different cell populations. Damage to retinal cells due to high dose gamma irradiation may be investigated with this technique, allowing researchers to understand the other effects of gamma irradiation intended for the destruction of cancerous cells. In this application, the use of an adequately restrained awake mouse would allow the cornea to remain clear and extend possible imaging time to the eight hours needed to track cell migration and homing.

Bone marrow transplantation is a stem cell based therapy that is used to treat cancers of the blood system. For successful transplantation, the maximization of donor cell engraftment is key. Tracking these stem cells during the homing and engraftment process will allow researchers to characterize the environment that promotes donor cell survival and engraftment. Imaging of the skull over a 24 hour period is necessary to observe the cell migration and proliferation processes.

A holder that is able to keep the mouse still for an extended imaging period would enable the characterization of hematopoietic stem cell location and orientation during mitosis, and their homing process.

Sedation of the test animal changes the cerebrovascular perfusion [2] such that researchers are not able to obtain data on the effect of brain cancer, stroke, TBI, on brain activity in an awake mouse. Optical coherence tomography enables structural imaging and angiographic imaging. The ability to view cerebral vasculature may offer insights into tumor growth and inhibition of cancer therapies. A current avenue of research investigates the use of anti-angiogenic drug therapies to repair the vascular network destroyed by a tumor in order to improve the efficacy of follow up therapies[3]. One potential application of a new restraint device is to enable imaging of activity in awake animals. The structures of interest from the potential applications outlined above are summarized in Table 1.

TABLE 1: Structures of Interest for Proposed Biological Imaging Applications

Structure	Size	Units
Red Blood Cells	6-8	μm
Neurons and Dendrites	0.2 - 2	μm
Pericytes (Retinal Cells)	~0.7	μm
Capillaries	5-10	μm
Hematopoietic Stem Cells	12-25	μm

1.1.2 Imaging Techniques

The most commonly used imaging technologies and their resolution capabilities are summarized in Table 2.

Table 2: Imaging Techniques

Imaging Technique	Lateral Resolution	Axial Resolution	Units
Optical Coherence Tomography (OCT)	3	4	μm
Multiphoton Microscopy	0.207	0.814	μm
Adaptive Optic Scanning Laser Ophthalmoscope	0.7	2	μm
Spectral Domain OCT	2.4	1	μm

The resolution of each technique is sufficient to track and characterize the structures of interest outlined in Section 1.1.2. An example of multiphoton microscopy, the imaging technique with the best resolution, is shown in Figure 1.4 where it was used to capture cell activity in bone marrow.

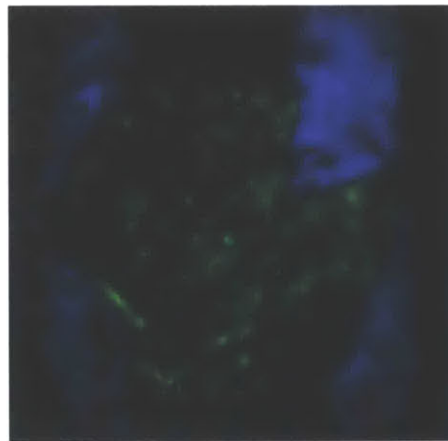


Fig 1.4: Cortical bone (blue) sits on top of a bone marrow compartment containing GFP+ cells (green) following intravital laser osteotomy [4]

However, high image resolution capabilities currently cannot be exploited due to the motion of the animal itself. Applying anesthesia simplifies this problem, as the only motion that needs to be constrained is that generated from heartbeat, breathing, and occasional convulsions. These motions range from tens of microns to millimeters, resulting in images that are degraded and blurred unless the animal can be restrained. A common technique is to use high frame rate imaging and post processing software to mitigate the effect of the mouse movement, however these

approaches are costly and time consuming. In addition, they are insufficient in the case of an awake animal or during a period of significant convulsions.

The ideal solution for generating clear high resolution images is to prevent motion of the mouse during the imaging period. A mouse holder capable of restraining motion over a long (24hr) time scale would:

- a) Enable imaging of micro tissue structures at high resolution
- b) Improve ability to track cell movement over longer imaging periods
- c) Enable study of physiological response to sensory input or therapy in awake animals

The restrainer design could be easily modified to constrain other animals or redesigned for access to specific parts of the body. An effective restraint device may also be used to perform surgeries or stabilize the mouse during healing.

1.1.3 Motivation for Device from Literature

The current limitation in many biological research studies is the movement of the mouse. As outlined above, the high resolution imaging techniques available are capable of capturing the structures of interest in sufficient detail. However, the movement of the mouse during awake or anesthetized imaging imposes serious limitations on the quality and type of data that may be collected during experiments. In the anesthetized case, one paper reported that “Movement caused by heartbeat, respiration and slow drifts prevented online improvement of signal to noise ratio by frame averaging.”[5] Another study focusing on ocular imaging also faced serious problems with mouse motion; “Eye motion in the anesthetized mouse was primarily from heart rate and respiratory artifacts that create ocular movements on the order of tens-of-microns”[6]. The z axis is particularly sensitive to movement, as it more difficult to correct images in post processing.

Researchers mention the devastating effects of mouse movement greater than a micron, saying that "tissue movement by as little as a few micrometers can render three-dimensional image stacks uninterpretable"[7].

1.1.4 Potential Impact of Device on Experimental Design

A mouse restraint device capable of holding a mouse in the same position relative to the imaging window and preventing movement greater than a micron would enable the experiments described above and decrease the amount of poor quality images due to movement artifacts that are unusable for data collection. A device that can reliably prevent fast movements of the mouse such as convulsions would enable researchers to extend their imaging session and view changes in physiology over a longer timescale.

1.2 Existing Restraint Methods and Limitations

As mice are a commonly used model for biological studies, there exist many restraint devices and techniques that restrict movement. In this section the existing options will be reviewed and their limitations discussed as the motivation for the design of a new device.

1.2.1 Prior Art: Stereotaxic Devices and Restraint Methods

Bone marrow and brain imaging both require a cranial window to be constructed. This process requires the skin on top of the head to be cut away, the skull removed (for brain imaging), and a clear protective layer applied to the exposed area. This surgery is performed with the anesthetized mouse in a stereotaxic holder or similar restraint device. The mice are allowed to recover from the surgery for at least a day before they are taken for experimental imaging. The majority of existing restraint devices and techniques are designed for work with anesthetized

animals and use micrometers or adjustable probes placed against the animal's skin for positioning and restraint.

Techniques designed for imaging of awake mice often use a metal plate glued to the skull around or near the cranial window. This metal plate is then rigidly fixed to the holder, preventing movement of the skull. The actual performance of these devices ranges from 1-5microns of skull movement, but there is also movement of the brain relative to the skull. Other techniques for collecting data from awake mice include rigidly fixing metal tubes to the skull above a predrilled hole, into which an optical or electrical probe is inserted for data collection. Examples of restraint techniques and their performance are shown in Figure 1.5. The dotted red line demonstrates the desired maximum displacement for the highest quality images.

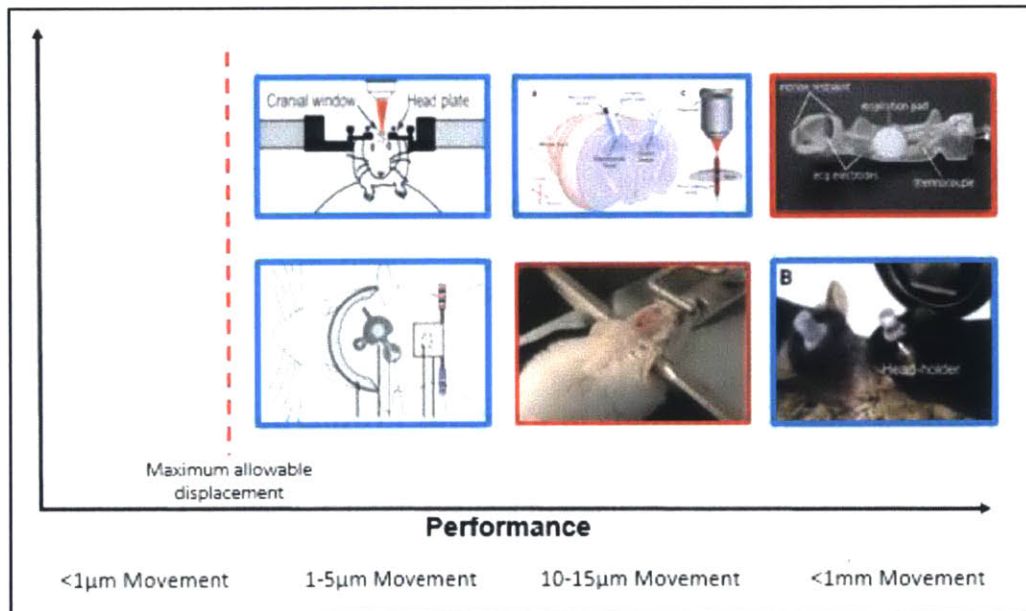


FIG 1.5: Current Restraint Devices for brain imaging with devices for awake mice outlined in blue and devices for anesthetized mice outline in red. References, left to right from top left: ([8] – metal plate fixed to skull, [9]- tubes fixed to skull, optical probes inserted , [10] – “body sleeve”, [11] – pole fixed to skull, [12]- stereotaxic device interfacing with nose and ears, [10] – head holder glued to skull)

The best performing awake mouse restraint techniques described and shown above involve rigidly attaching a fixture to the skull. This approach has two major limitations. First, they cannot

be used for bone marrow imaging because the cement used to attach a metal plate or other fixture to bone may be toxic to the cells and changes the physiological response of interest. Second, this approach requires additional surgery and recovery time for the mouse to heal before imaging can take place. One of the functional requirements for the design of a new restraint device is that it does not require adhesive of any sort being applied to the skull. The cements and adhesives normally used to fix the metal to the bone are toxic to the surrounding cells, and thus affect the experimental results. This limitation creates the need for a fixation method that does not interface with the skull itself.

In order to meet this requirement, the restraint device designed in this thesis will make contact only with the skin, and will not require any surgery beyond that necessary to access the imaging area. In order to design this device, more information about the material properties of the tissue surrounding the skull are needed. After a literature review, additional testing will be done to validate published values and establish a range of values for tissue properties not found in the literature. Then the feasibility of an approach that makes contact with only the skin will be investigated for both the awake and anesthetized restraint cases.

1.2.2 Performance and Limitations of Previous Prototype

A mouse restraint device for anesthetized animals was developed by Culpepper et al [13]. The device consists of three contact points with the skin of the mouse's head. The prototype and its performance are shown below.

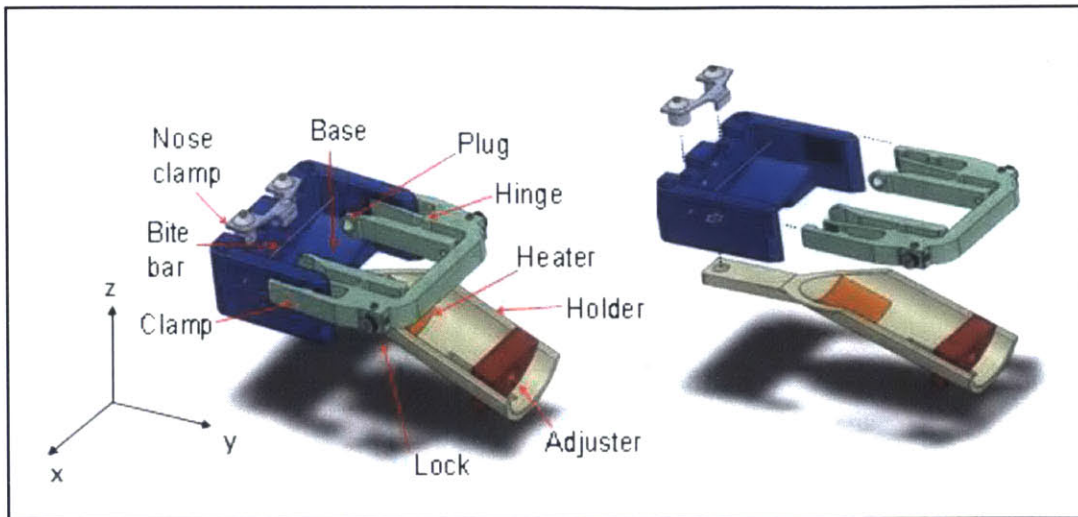


FIGURE 1.6: Prototype designed by Culpepper et al

The initial (anesthetized mouse) prototype developed by Culpepper et al. has 4 contacts, 1 next to each ear, the bite bar, and the nose clamp. Exact kinematic constraint requires the number of constraints to equal the degrees of freedom, which is six for any rigid body.

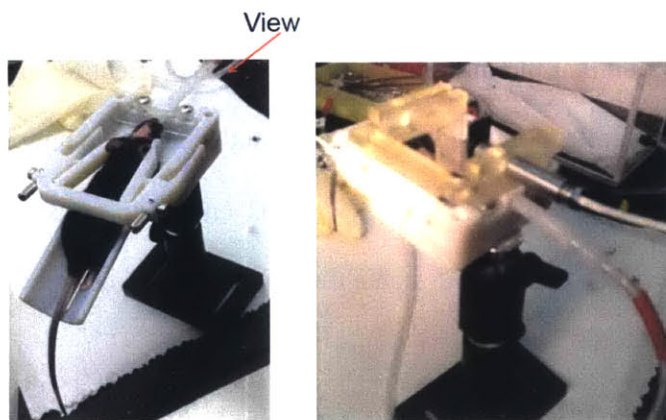


Figure 1.7: Experimental Set Up Without (A) and With (B) Capacitance Measurement Probe. Arrow in (A) Indicates View Orientation Seen In (B)

For an anesthetized mouse the holder was able to keep skull displacement to less than a micron over a period of several minutes. Jumps could be seen in the data corresponding to heart beat ($\sim 0.02\mu\text{m}$) and respiration ($\sim 0.1\mu\text{m} - 0.2\mu\text{m}$).

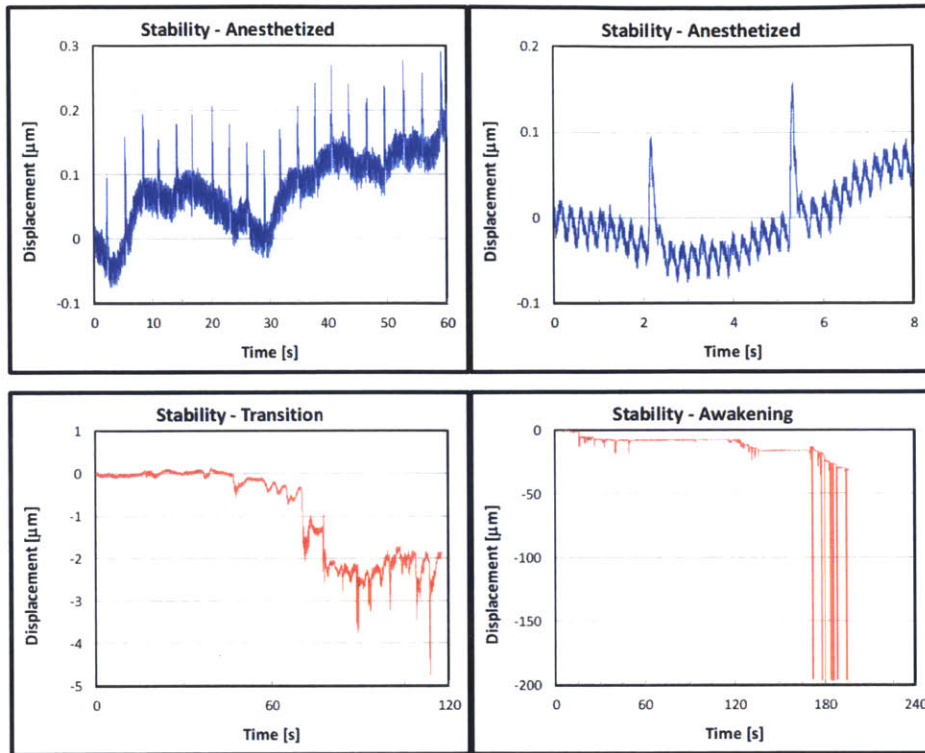


Figure 1.8: Motion of Skull in Z Axis While Mouse is Anesthetized (A) and (B), Data in (B) is Close-up View of Data in (A) Showing Induced Motions Due to Breathing and Heartbeat. Motion of Skull While Animal is Waking (C) and Fully Awake. From SBIR Proposal, Culpepper et al.[13]

The results demonstrate that the initial prototype was insufficient to constrain the mouse when it is awake. No data was collected in the x or y axes, so it is unknown how well this device restricted movement in those directions. As this device was unable to constrain an awake mouse, the feasibility of doing will be explore through a theoretical model, outlined in Chapter 2 and detailed in Chapter 5.

1.3 Requirements for Improved Restraint Device

The requirements for the design of an improved restraint device are derived from the limitations seen in existing devices and user needs based on discussion with research scientists who work with laboratory mice on a daily basis.

1.3.1 Functional Requirements for Restraint Device

The functional requirements for the awake mouse restraint device are given in Table 3:

Table 3: Restraint Device Functional Requirements

Metric	Required	Desired	Units
Slow Drift	10	2	% of image
Mouse Movement (x, y)	<1	<1	micron
Mouse Movement (z)	<0.7	<0.7	micron
Geometry	<5x5	<5x5	cm
Applied Force Accuracy	+/- 1	+/-0.5	N

Slow Drift: The change in position of the imaging area with respect to the lens during the entire imaging period, which may be anywhere from two to twenty four hours. Temperature fluctuations, mouse movement, and device creep may lead to drift.

Mouse movement: The point spread function (PSF) of the multifocal/confocal imaging setup determines the functional requirement for the system. This imaging technique scans the area of interest with a laser beam, recording one pixel at a time while the beam is moving. It should be noted that the axial (z axis) movement is the direction of section and therefore the most difficult to correct in post processing, explaining the lower allowable displacement.

Applied Force Accuracy: The maximum allowable force to prevent breaking the skull will be different at each contact location based on skull thickness and geometry in that area. Therefore it

is necessary for the force applied at each location to be known or limited, to prevent injury to the mouse.

1.3.2 Physiological Properties of Laboratory Mice

In order to successfully design a device to interface with laboratory animals, their physiological properties must be understood. The design of this restraint device, while applicable and scalable to other laboratory animal subjects, is focused on mice. In order to interface with the mouse skull and surrounding tissue, it is necessary to characterize their material properties. The parameters needed for the device design are listed in Table 1.4.2, some of which do not have a constant and/or currently known value and so will be further derived or found through testing in succeeding chapters.

Table 4: Laboratory Mice Physiological Properties

Parameter	Value	Units
Heart Rate[14]	632 +/- 51.3	Beats/min
Respiration [7]	163	Breathes/min
Weight [7]	18-35	grams
Skin Stiffness	Function of strain	Pa
Muscle & Fat Layer Stiffness	Function of strain	Pa
Force to crack skull	Dependent on location	N
Force generated by mouse	Unknown	N

As the feasibility of restraining both anesthetized and awake mice will be explored, we will outline the considerations necessary for each case. Anesthetized animals must be constantly monitored to ensure their airway is not blocked by the restraints and they are breathing at the correct rate, about one breath per minute. Anesthetized mice must also be kept at a body temperature of ~37C, which requires the use of a heating element during all testing. When using awake animals in laboratory experiments, it is critical that they be kept comfortable and pain free at all times. In addition, the mouse must not be injured or put at risk of pain or injury by the setup.

These conditions must be met in order for an experiment to be approved by the research institute's Committee on Animal Care. Therefore in addition to designing a setup that prioritizes mouse comfort, it may be necessary to include a conditioning period in the preparation process in order to attain mouse cooperation in an imaging setup that restricts movement. This may include placing the mouse in the setup for short time periods to familiarize them with it, providing milk as a reward, and continuing this procedure until the mouse is comfortable enough to stay in the setup for the necessary imaging time. This conditioning procedure takes about two weeks to build up to two hours in the current awake imaging setups, which constrain mice by clamping onto a rigid metal plate glued to their skull.

1.4 Thesis Summary

The objectives of this thesis are to:

- 1) Characterize the critical material properties of mouse soft tissue and bone
- 2) Quantify the performance of a constraint system based on input parameters
- 3) Select a constraint method and apply it to the design of a mouse head restraint device.
- 4) Determine the possible performance of a mouse restraint device and whether it will accomplish the goal of sub-micron level movement for the awake and anesthetized cases.
- 5) Design a restraint device for optimized performance, and compare its performance with that predicted by the model.

The first chapter of this thesis has been a discussion on the motivation behind this work as well as a summary of prior work and existing devices. Chapter 2 will discuss the selection of a constraint method and the material properties needed to refine this model and determine its efficacy. Chapter 3 discusses the design of an experimental setup to measure tissue properties and determine whether

shear stiffness may be neglected in the constraint model. Chapter 4 details the results of these experiments and compares them to those found in the literature. Chapter 5 develops the theory to characterize the performance of a constraint system, and details the specific inputs for the mouse restraint case. Chapter 6 outlines the design of the awake mouse restraint device and Chapter 7 discusses its performance. Chapter 8: Summary and Future Work recaps the work done in this thesis and discusses future applications and areas for further work.

CONSTRAINT METHODS, SYSTEM MODELING, AND MOUSE PROPERTIES

Chapter 2 discusses the possible approaches to constraint considered and the selection of the kinematic constraint method. The system model is developed in Section 2.2, and the assumptions made in order to predict behavior are eliminate terms are detailed in Section 2.3. In Section 2.4 the material properties of mice relevant to the chosen constraint method and system model are explored through a literature review, and challenges are considered. The force the mouse can generate, one of the critical elements to understanding system performance, is approximated in Section 2.5 using values from the literature.

2.1 Design Constraints

The Functional Requirements for the design of the restraint device were outlined in Section 1.4.1. In addition to these requirements, several limitations were imposed on the nature of any interface with the mouse. First, nothing could be glued or attached directly to the skull. The glues normally used to accomplish this are toxic to cells, and this affects biological activity in the area of interest, particularly in bone marrow imaging[15]. Secondly, this type of restraint requires prior surgery and a recovery period for the mouse. Finally, this technique has been attempted with some

success before [8], but required the mouse to be constantly moving, which is infeasible for a 24hr imaging period.

2.1.1 Contact Options

Several approaches were considered for restraint before the compressive skin contact was selected. Adhesive, rigid connection to the skull was dismissed due to the need for added surgery and the adverse effect of adhesives on experimental results due to toxic effects. Non-adhesive, direct contact with the skull, for example with pins that puncture the skin as used to fixture human skulls for imaging, was also considered but dismissed due to the pain and discomfort caused to the animal and the potential to damage the brain if the sharp contact were to puncture the skull. Puncturing the skin is not something that the animal can be conditioned for, as it causes pain each time.



FIGURE 2.1: Titanium human skull pin used for positioning the head during imaging and radiation therapy. The pins puncture the skin and contact the skull to hold it in place. [16]

Once the approach of removing the skin were eliminated, the type of contact with the skin was considered. Skin exhibits different material properties in tension and compression, with the tensile modulus on the order of megapascals at 25% strain, while the compressive modulus remains in the kilopascal range. Tensile restraint in which the skin is pulled taught was considered, but eliminated due to the high creep that occurs in tensile loading of nonlinear viscoelastic materials

such as skin[17]. As a result, compressive contact with the skin was selected as the contact approach, and used to develop a constraint model for the system.

The approach developed in this thesis assumes that any contact that occurs must be with the outer surface of the skin. This presents some complications, as biological tissue is a nonlinear elastic material, meaning that its stiffness changes as a function of strain. In order to characterize the best possible performance of a system it is necessary to know how the stiffness changes as a function of strain, and so further exploration of the material properties of the muscle and skin tissue will be performed and discussed in Chapters 2.4 - 4.

One of the other major obstacles to brain imaging is the relative motion of the brain and the skull. Even if the skull is fixed such that no significant motion is observed, the brain may move within the skull itself due to the mouse's movement. This is because the brain is suspended in cerebrospinal fluid) which acts to cushion the brain and protect it from impact. Any contact with the brain should be avoided to prevent damage and compromising the experimental results. For bone marrow and retinal imaging (two of the three proposed applications), this is not an issue. Without a satisfactory way to address the problem of brain movement within the skull, the restrainer design will focus on minimizing the motion of the skull itself. For bone marrow imaging, one of the proposed applications, this problem does not exist as the skull itself is the area of interest.

2.1.2 Active vs. Passive Constraint

To achieve better constraint performance an active mouse restrainer with actuators and position sensors was considered as a possible approach. Theoretically, an active device would read the position of the skull using a capacitive probe or other sensor, then apply a force, moving the skull to correct for any displacement from the original desired position. For the case of a rigid

body surrounded by a deformable layer, where contact may only be made with the outer surface of the deformable layer, it was determined that an active system would hold no advantage over a passive system for several reasons:

- 1) A position sensor located on the skin surface (outer surface of the deformable layer) would not be able to provide an accurate measure of the skull position. This is due to the ability of this outer surface to move independently of the skull, as a function of the force applied. The position sensor also cannot be located on the top of the skull (the area of interest) because it would interfere with the imaging setup or viewing path.
- 2) If each constraint contact with the deformable layer is already set to the maximum allowable force (determined by the material strength and geometry of the interior rigid body), any actuator acting on the surface would not be able to apply more than this maximum force, therefore it could not exert a corrective force on the body. It is advantageous for the contact force to be maximized initially to minimize displacement of the skull.
- 3) If an actuator in contact with the skin was allowed to apply a higher than maximum force in order to correct for position error, it would not necessarily result in the correct magnitude of corrective displacement - due to low tissue stiffness the majority of deformation would occur in the tissue itself and not be transmitted to the skull.

Due to the lack of advantages and feasibility in implementing an active constraint system, a passive system approach was selected. The passive system is also lower in cost, complexity, and size, further advantages in the proposed laboratory setting.

2.2 System Model

In order to fully constraint the mouse head, each degree of freedom must be constrained.

Figure 2.2 shows the mouse skull and each of its six degrees of freedom.

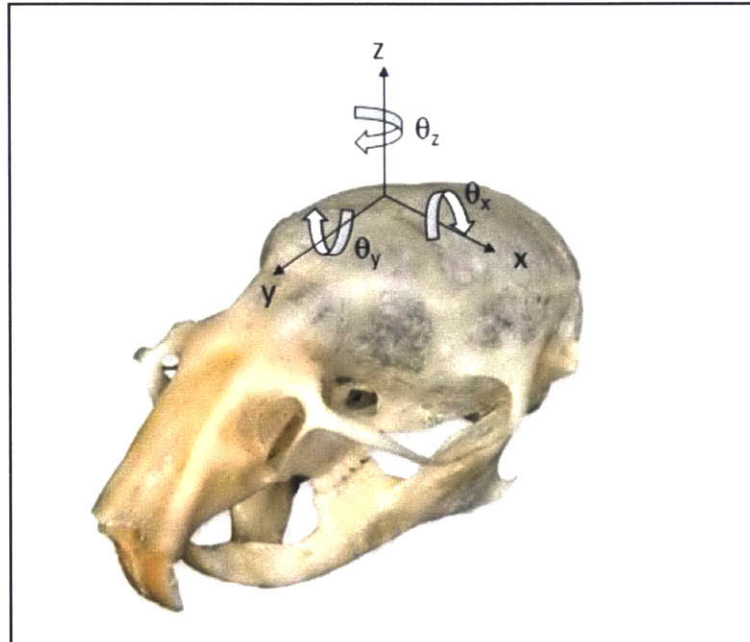


FIG 2.2: Mouse skull and associated degrees of freedom [18]

Although we are interested in restricting the movement of the skull, since the restraint device is restricted to contact only with the skin it is critical to model the interaction of the contact with the mouse. Figure 2.3 shows the system modelled as several springs in series, where what is desired is minimal displacement of the skull, X_I .

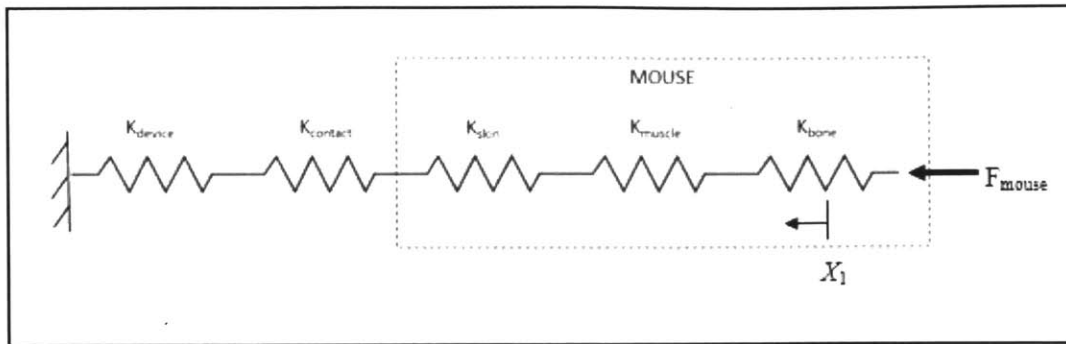


FIG 2.3: Spring Stiffness Model for Constraint System and Mouse

Using this model, the displacement of the skull, X_1 may be predicted by finding the equivalent system stiffness:

$$k_{eq} = \left(\frac{1}{k_{device}} + \frac{1}{k_{contact}} + \frac{1}{k_{skin}} + \frac{1}{k_{muscle}} + \frac{1}{k_{bone}} \right)^{-1} \quad (1)$$

$$X_1 = \frac{F_{mouse}}{k_{eq}} \quad (2)$$

To calculate this equivalent system stiffness, values for each spring element must be found. The stiffness of the bone and device may be easily found as the Young's Modulus for ABS, aluminum (potential device contact materials), and bone is known. The stiffness of the skin and muscle is nonlinear, and the resulting changes to the above model will be discussed further in Section 2.2 and Chapter 5. The contact stiffness value is unknown and will be dealt with in Section 2.3.4.

2.3 Contact Stiffness

2.3.1 Hertzian Contact Stiffness Overview

Hertzian Contact Theory is used to determine the contact stress for two bodies between which no tension force due to adhesion exists. The Hertzian model assumes that some small

deformation of each body occurs at the contact area, but that this area is small in comparison with the characteristic dimension of each body.

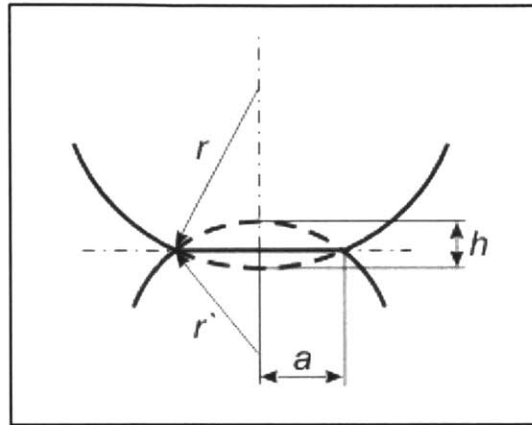


Figure 2.4 Relation between contact area radius a and penetration depth h in deformed state for hertzian contact model. [19]

The criteria necessary for the application of Hertzian Contact Theory are outlined in Table 5 and compared to the mouse restraint case to determine whether this theory may be applied to find a value for the contact stiffness.

Table 5 Hertzian Contact Theory Applicability

Hertzian Contact Criteria	Mouse Skin Contact Case	Criteria Met?
Two non-conforming surfaces	One conforming (skin), one nonconforming (contact)	No
Each body considered elastic half space	Deformation area is small compared to area of surface	No
Surfaces are Frictionless – only normal pressure exists	This is an idealization for any case – can't actually be true	Unknown
Strains are small and within elastic limit	Strains are within elastic limit, but large ($\gg 0.01$)	No

The criteria for Hertzian Contact theory are not met, so this model cannot be used to characterize the contact stiffness. Instead, finite element analysis will be used to determine the effect of contact stiffness on the overall stiffness of the system.

2.3.2 FEA Model of System

Finite Element Analysis was utilized to demonstrate that the contact stiffness in the case of contact>skin>bone may be neglected. The system stiffness when the contact and bone components were modeled as perfectly rigid closely approximates the system stiffness when those components were assigned their actual stiffness ($E=69\text{GPa}$ and $E=8\text{GPa}$ respectively).

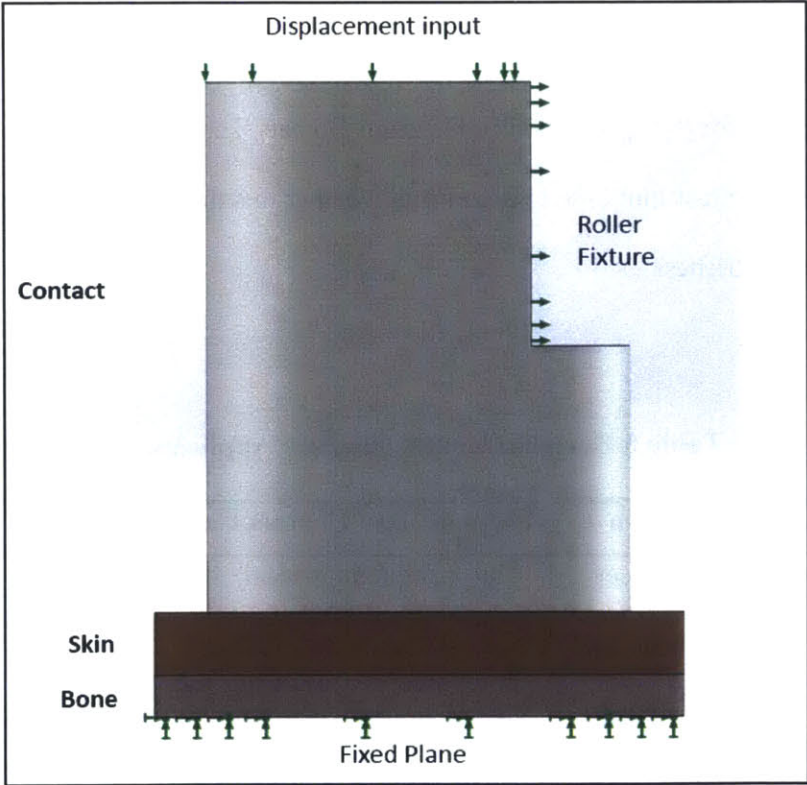


FIG 2.5: Setup for FEA simulation. Displacement condition applied at top face of contact. Bottom surface of 'bone' layer fixed in place, roller condition applied to contact side face to limit it to one degree of freedom.

For both tests, the elastic modulus of the skin was specified by a nonlinear curve with modulus coefficient in the range found in the literature. The bone and skin layer thicknesses were set to 400 and 600 microns respectively, reflecting values measured in laboratory mice. For test 1 the actual elastic modulus values of the bone and contact parts were used. For test 2 the bone and contact part materials were modeled as infinitely rigid, to reflect the case in which contact stiffness would be nonexistent as all deformation must occur in the skin layer.

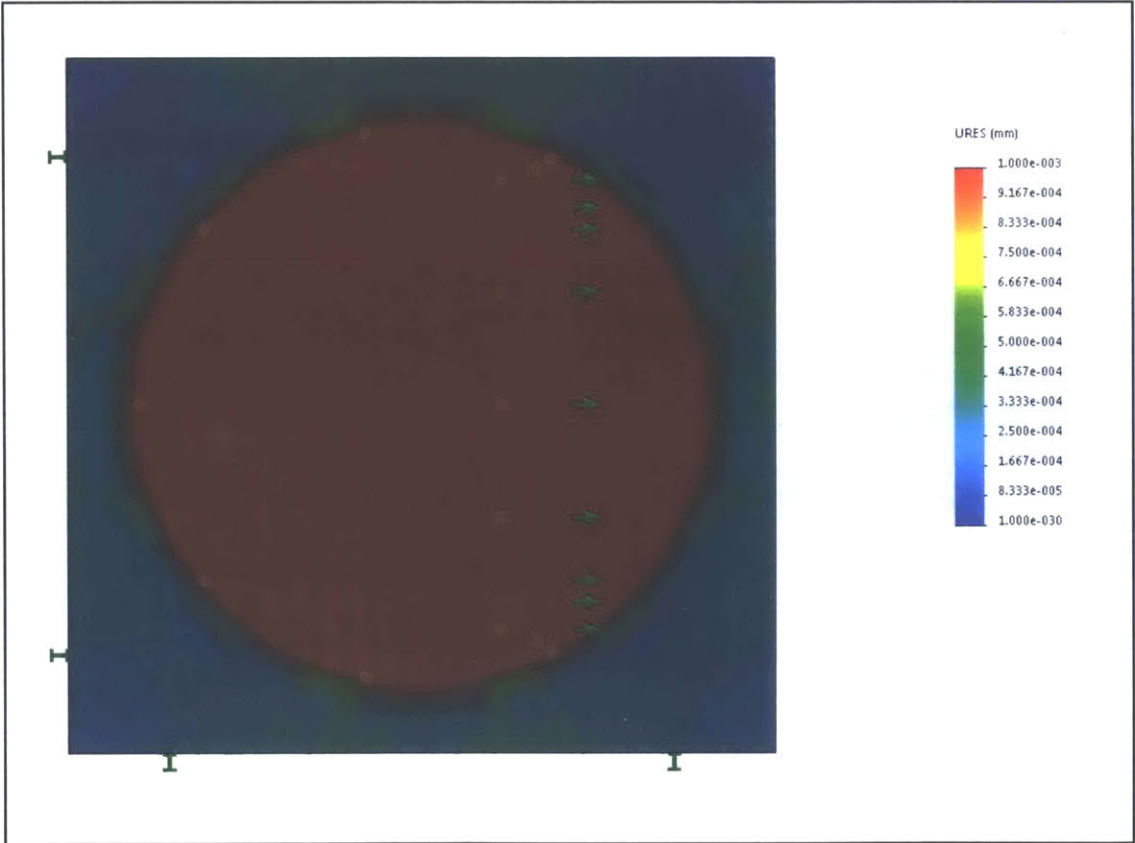


FIG 2.6: FEA Results for Test 1 (contact and bone modeled with real world values) showing displacement of top surface of skin. A displacement of 0.001mm was applied to the top of the contact

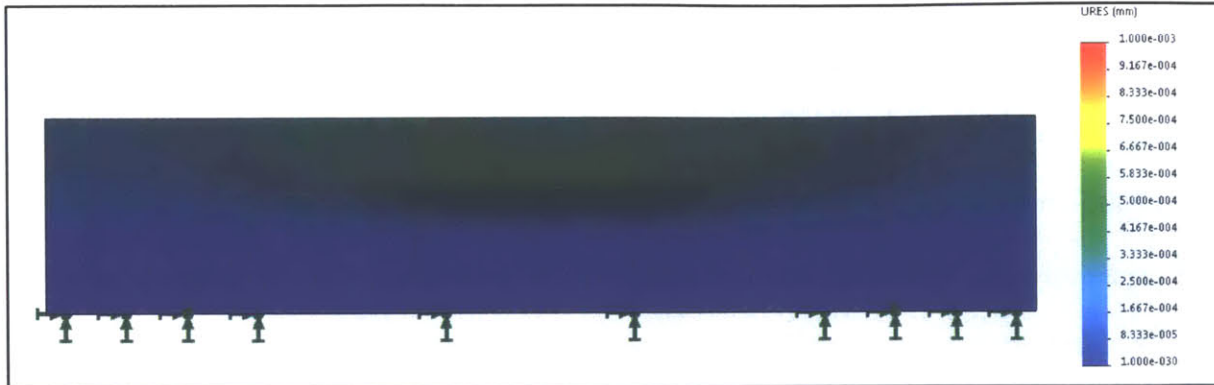


FIG 2.7: Side View of Skin and Bone Displacement for Test 1: Displacement of outside edge of skin layer is on order of 0.0005mm, displacement in bone layer approaches zero (order of $1e-30$ mm).

The resultant force, measured at the skin interface with the contact was divided by the averaged displacement of the skin layer over the contact layer to find the system stiffness, which is summarized in Table 6:

Table 6: FEA System Stiffness Results

Test	Bone E	Contact E	Stiffness (N/mm)
1) Mouse Restraint	8 GPa (Bone)	69GPa (Aluminum)	$7.98e-8$
2) Idealization	infinite	infinite	$5.21e-8$

As there is less than a factor of two difference between the stiffness values for the idealized and actual case, this means that the deflection of the bone and/or contact contribute very little to the stiffness of the system as a whole. Therefore, the contact stiffness can be neglected in the system model.

Chapter 2.3 has outlined the assumptions necessary for the application of kinematic constraint theory, and determined that the contact stiffness can be neglected. In future chapters kinematic constraint theory will be applied to the design of a restraint device.

2.4 Material Properties of Mouse Tissue

In the rigid body/deformable layer model, the mouse head application consists of a deformable layer composed of all tissue on the surface of the skull. The muscle can be seen when the skin is removed, demonstrated in Figure 2.8:



FIG 2.8: Muscle visible in cheek area once skin is removed

The skin has different properties in tension and compression. Wang et al [20] found the tensile modulus of mouse skin at 20-30% strain to be $\sim 6\text{MPa}$ while the compression modulus at the same strain was only 32KPa. However, pulling the skin in tension was ruled out as an approach to constraining the mouse for two reasons. First, putting the skin in tension may cause pain, as well as plastic deformation of the tissue. Second, the skin is capable of undergoing tensile creep under a constant force, so it would be difficult to accurately maintain a constant skull position.

2.4.1 Mouse Muscle Layer Properties

Several studies have nominally characterized the elastic properties of muscle tissue. Chin Wing Zot et al. used ultrasound elastography to measure the elastic modulus of muscle in live subjects[21]. However, the study did not specify or measure the induced strain during measurement, and the values varied from 8KPa - 46KPa depending on the indentation of muscle

layer by the transducer. Another study tested the nonlinear stress strain relationship in bovine muscle samples, but did not induce strains greater than 0.16 [22].

Kruse et al. stressed rabbit skeletal muscle to 40% strain, and published values enabling curve fitting of the stress-strain curve. This work also found the tissue modulus to be highly dependent on the orientation of muscle fibers [23]. The values published in these papers were used to verify the modulus found for mouse muscle tissue during testing presented in Chapter 4. However, no literature was found discussing the failure criterion or behavior at extremely high strains for muscle or skin tissue under compression.

2.4.2 Mouse Skin Properties

The skin is composed of the epidermis and dermis, with any fat included in the dermal layer. The thickness of the skin varies depending on the mouse's age, the anatomical location, and the stage of the hair cycle [20]. While the elastic modulus and skin thickness has been quantified for mouse skin from various body locations by Wang et al, no testing of facial skin has been performed, nor has the stress-strain curve been explored beyond a maximum stress of 71 KPa. The mean value and range of the skin thickness and modulus will be discussed and tested in Chapter 4, then compared to values published in the literature. These values will enable the prediction of constraint system performance.

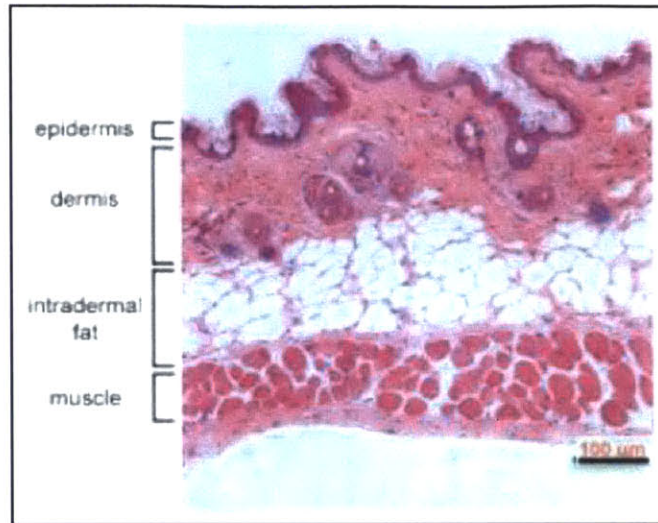


FIG 2.9: Skin layers in wild type mouse [24]

Skin is a nonlinear viscoelastic material, meaning its stiffness changes as a function of strain and strain rate. Since the performance of the device is dependent on the stiffness of the skin at each contact location, performance is directly correlated to the Force applied. Equation 3 describes the nonlinear stiffness curve (slope equals Young's Modulus) is

$$\sigma = \sigma_T(e^{q\varepsilon} - 1) \quad (3)$$

Where σ_T is the threshold stress, defined by the threshold force at which the force is said to be significant (and a function of actual tissue resistance and not measurement error or drift). Wang et al. and the Instron testing performed for this thesis (Chp 4) use a σ_T value of $\frac{F_T}{A}$, where $F_T = 0.01N$.

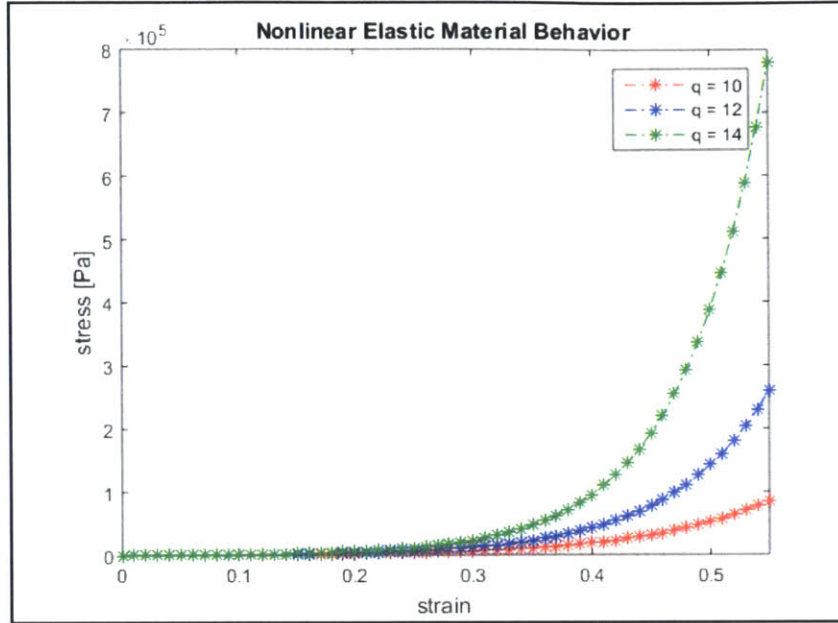


FIG 2.10: Example of stress-strain curve for nonlinear elastic materials with varying moduli coefficient, q .

FIG 2.10 shows an example of the stress strain curve for a nonlinear elastic material. The young's modulus may be found for a given strain by taking the slope of the line for a small delta around that strain.

$$E = \left. \frac{\Delta\sigma}{\Delta\varepsilon} \right|_{\varepsilon} \quad (4)$$

Viscoelastic materials exhibit both viscous and elastic properties as a function of time, meaning that the relationship between stress and strain is time dependent. According to the Kelvin Voigt viscoelastic model, when a constant stress is applied, the displacement of the material will approach the displacement for a pure elastic material. The strain for this case of constant stress decays with time and is represented by

$$\varepsilon(t) = \frac{\sigma_0}{E} (1 - e^{-\lambda t}) \quad (5)$$

Where λ is the rate of relaxation, and η is the viscosity of the material.

$$\lambda = \frac{E}{\eta} \quad (6)$$

For the case of skin compression relevant to the design of a mouse restraint device, either a constant force or constant displacement will be applied to the mouse. Under a constant stress a viscoelastic material may exhibit creep (an increase in strain over time), but will approach the displacement for a pure elastic material. Under a constant strain the material may experience stress relaxation, but the final displacement is the parameter of importance, which will not change. Therefore, because our time scale is large and we are concerned only with the final displacement of the material, viscoelastic effects will be neglected.

2.1.3 Mouse Bone Properties

It is necessary to know the elastic modulus and yield strength of bone in order to determine the maximum contact force and how the bone layer should be classified in the system stiffness model. The properties of the mouse skull were inferred from published values of human and rat bone material properties, as all skulls are made from mineralized osseous tissue. Testing of human cranial bones found an elastic modulus range of 10.3GPa - 22.1 GPa[25].

Mao et al. investigated the material properties of adult rat skull using three point bending tests. The average skull thickness was found to be 0.572mm, and the elastic modulus found to be 5.917 GPa with a standard deviation of 0.763GPa for slow loading conditions (most similar to our application at .02mm/s) vs 9.486GPa fast at 200mm/s. Therefore, a value of ~6GPa will be used in the system model

2.1.4 Summary of Material Properties

Based on the reported stiffness values in the literature, and the results of material testing with the setup described in Chapter 3, each of the major layers is classified as either deformable or rigid. Rigid layers are at least an order of magnitude stiffer than deformable layers, and are assumed to be stiff in the system compliance model, and the stiffness of the deformable layers as a function of applied force used to characterize the system performance.

Table 7: Classification of Tissue Layers

Layer	Nominal Elastic Modulus	Constant Modulus?	Classification
Skin	3KPa	No, function of strain	Deformable
Muscle	2KPa	No, function of strain	Deformable
Bone	4-12 GPa	Yes	Rigid

The skin and muscle layers are classified as deformable while the bone is classified as rigid because their elastic moduli are at least 3 orders of magnitude apart at all times. In order to fully develop the system model it is necessary to characterize the material properties of the muscle layer, as values found in the literature did not specify the strain they were measured at [21] or no testing was done for strains beyond 0.16 [22]. A setup will be designed to test the young's modulus of mouse tissue layers. This setup will also test the shear stiffness of the tissue in order to determine whether or not it may be considered negligible in the system model. A table with modulus and thickness values for each deformable tissue layer, including testing results and published values is provided in Chapter 4.5.

2.5 Force Generated by Mouse

In order to design a constraint system and predict its performance, it is necessary to understand the loads it will take. The force that the mouse applies due to heartbeat and respiration

is difficult to characterize, but the maximum force due to convulsions and attempts to escape can be estimated.

The linear head acceleration of a rat head has been measured in the range of 1.5g's - 2g's [26]. Another study by Venkatram[27] measured the maximum acceleration of a rat/mouse? To be 1.5 g's during normal behavior. One study assumed a maximum acceleration of 5g's, three times that seen in normal exploratory behavior[11], confirming the assumption of 1.5g's - 2g's as the range of acceleration of a mouse.

To calculate the maximum force a mouse may apply, a conservative estimate of 5g's will be assumed for acceleration. The average mouse has a mass 20g-40g[14].

$$F = ma \tag{7}$$

$$F_{mouse} = (.04kg) \left(9.8 \frac{m}{s^2}\right) (5) = 1.96N \tag{8}$$

The constraint device will be designed and its performance predicted based on this worst case estimate. Testing of the device itself will allow for actual measurements of mouse force.

DESIGN OF MATERIAL TESTING SETUP

This Chapter presents the design of a material property testing system, including mechanical and electronic elements. Functional requirements are presented in Section 3.1. Section 3.2 discusses critical subsystems and the design and selection of components. The system error is presented in Section 3.3, and the designed device is compared to the functional requirements in Section 3.4.

3.1 Functional Requirements for Testing Setup

In order to determine the contribution of the perpendicular stiffness, confirm the literature values for skin modulus, and find a modulus for the muscle layer, a testing setup was designed. The goal of the setup was to test the skin stiffness in two directions corresponding to two different modes of mouse movement; axial (1) and shear (2), as shown in Figure 3.1.

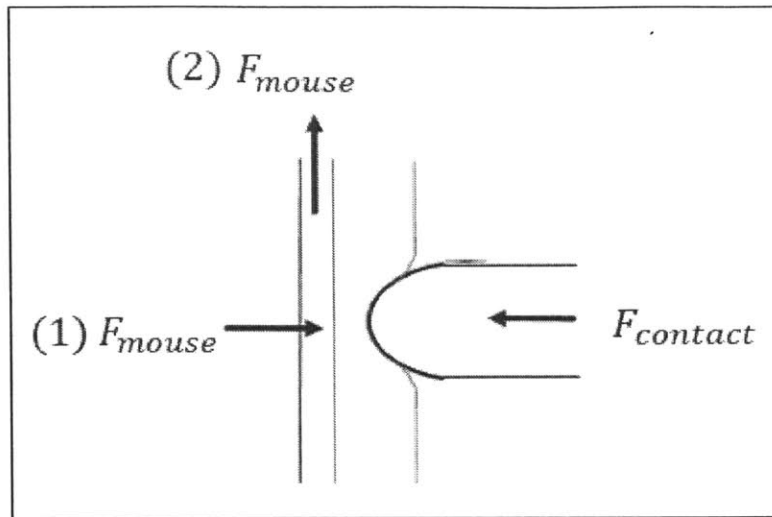


FIG 3.1: Modes of mouse movement in relation to contact

In order to test these stiffness, a high degree of accuracy was necessary for both the actuator input and position reading in each axis. The functional requirements for the system are summarized in Table 8:

Table 8: Functional Requirements for Material Testing Setup

Property	Required Metric	Desired Metric	Units
Force Control	Within +/- 0.05N	Within +/-0.01N	N
Dimensional Stability	<1	<1	μm
Displacement Resolution	<100	10	nm
Strain Rate	Constant +/- 0.5	Constant +/- 0.1	mm/s

Force Control: The force control accuracy is the maximum error of the absolute value of the input force. The force control resolution is the

Dimensional Stability: The position of machine components relative to one another should remain constant to within one micron during the duration of a test, which lasts approximately one minute.

Displacement Resolution: The smallest increment of translation measurable in each axis of interest.

Strain Rate: The rate at which the skin is compressed must be constant, as due to its viscoelastic nature this could affect the measured value of stiffness during a test.

3.2 Mechanical Design of Setup

The material property testing setup is composed of two actuation axes to test shear and axial stiffness. The actuation mechanism for each axis was selected based on the range of motion, input force range and accuracy needed.

3.2.1 Axis Actuation

To test shear stiffness, a force controlled actuator is necessary in the x axis in order to apply a constant force to the tissue. A voice coil actuator was selected and the input force controlled using a LabView script. In order to transfer the actuator force to the material being tested with minimal frictional losses, an air bearing guide for the shaft was implemented. The load path from the voice coil to the mouse location is shown in blue in Figure 3.2.

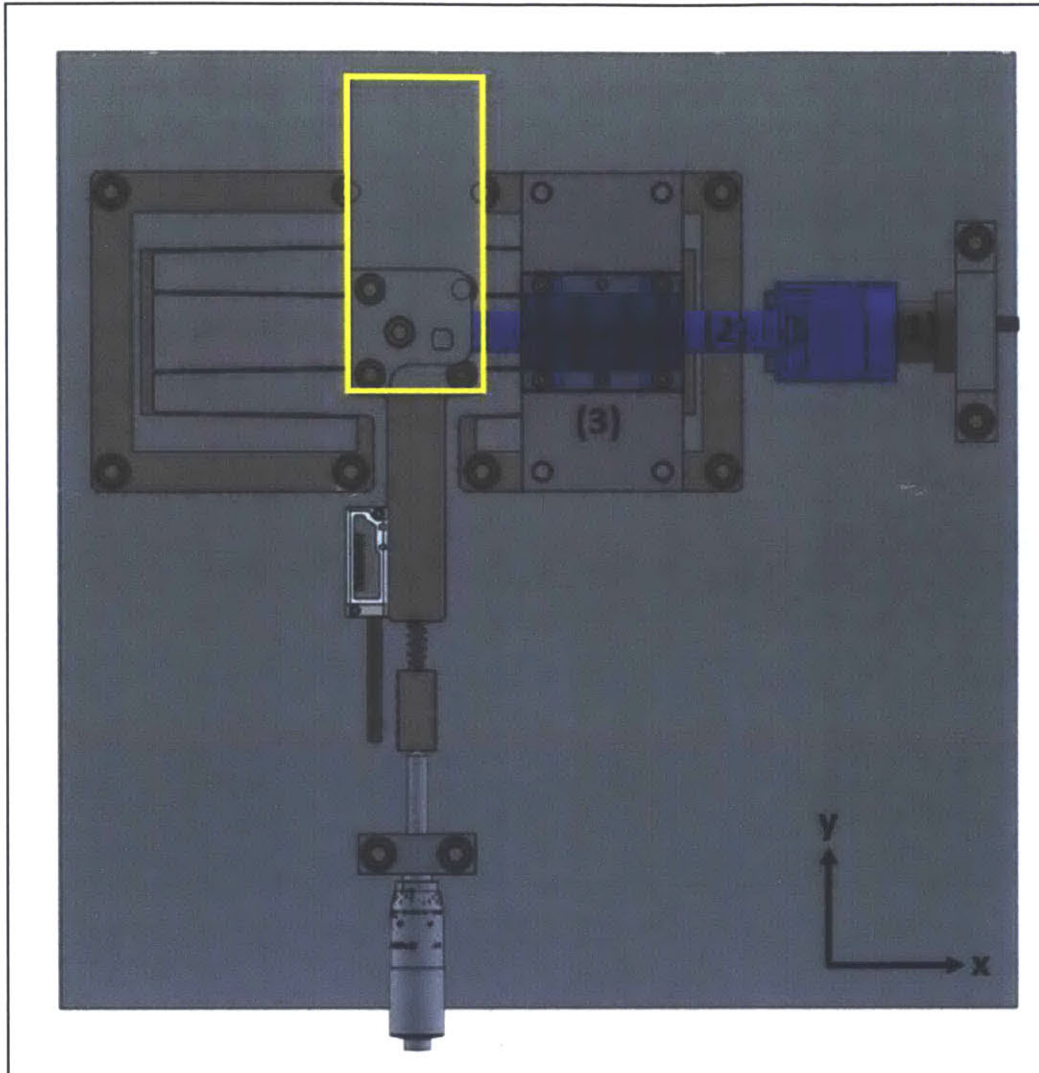


FIG 3.2: Voice coil actuator (1), shaft (2), and air bearing guide (3) shown in blue. Mouse location represented by yellow box.

For the axial stiffness test, the force applied by the voice coil follows a ramp function until the maximum force is reached. The displacement of the actuator shaft is measured and recorded throughout. For the shear stiffness test, the voice coil actuator is used to apply a constant force against the fixed mouse skull. Then, a force is applied in the y axis by moving the micrometer a set amount, compressing the spring and applying a force to the single degree of freedom four bar

flexure where the mouse is attached. Then the displacement of the flexure (and therefore mouse or tissue) is measured

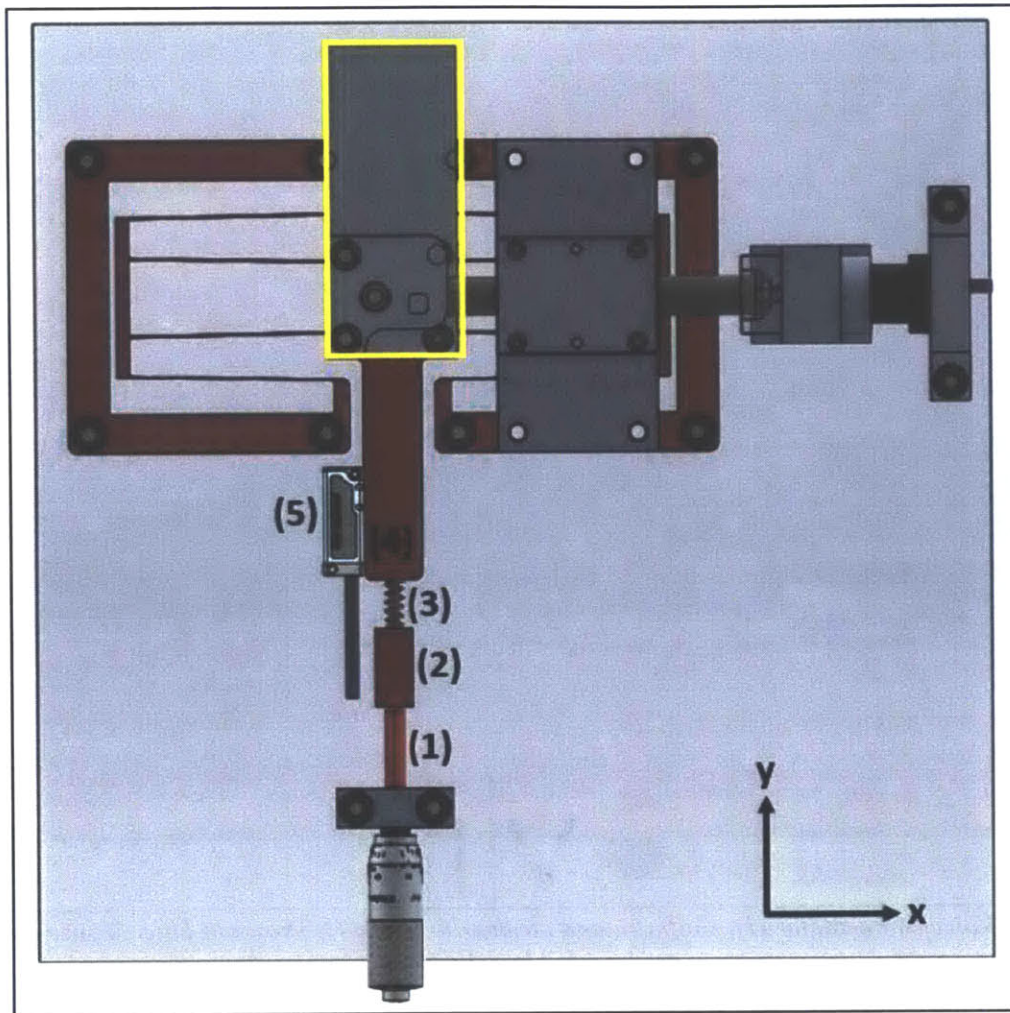


FIG 3.3: Elements that control travel in the y axis. The micrometer (1) position is adjusted, pushing the block (2) forward and compressing the spring (3), which applies a force to the four bar flexure (4), moving the mouse plate (yellow outline). The position of the flexure and attached mouse plate in the y axis is measured with the position sensor (5).

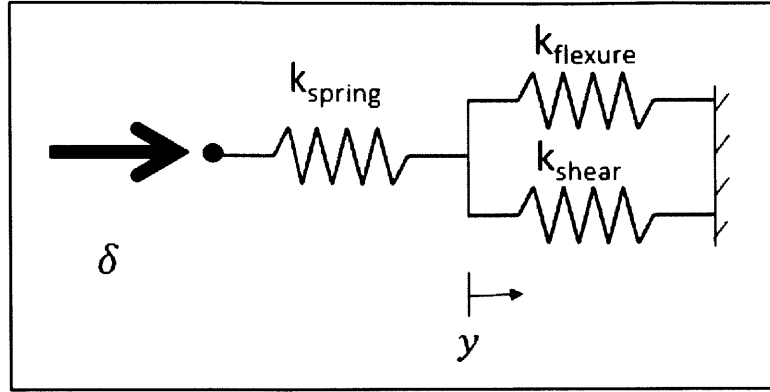


FIG 3.4: Schematic of load path and displacement of elements in y axis

$$\sum F = k_{spring}(\delta - y) - (k_{flexure} + k_{shear})y = 0 \quad (9)$$

$$k_{shear} = \frac{k_{spring}(\delta - y) - k_{flexure}y}{y} \quad (10)$$

The input displacement δ was set to change in steps of 0.01mm, and the displacement x measured by a linear encoder. The spring constants of the push spring (6.9027 N/mm) and flexure (3.158 N/mm) were measured using an Instron machine before the setup was assembled. Using these values, the value of the shear stiffness could be calculated for every input displacement.

In order to accurately measure the force applied and the resultant displacement, a low friction drive was desired for each axis. For the y drive system, the functional requirements for travel were travel ≥ 3 mm with less than 10N input force, and a safety factor of 2 for yield at a displacement of 3mm from initial position. The resolution and accuracy of this travel needed to be on the order of 0.1 μ m. The single degree of freedom plate to which the mouse was rigidly fixed was achieved with a four bar flexure. The flexure has a single degree of freedom (y), and is stiff enough in x and z such that it will not deflect more than one micron under the expected 5N load applied during a test ($k \geq 5(10^6) \frac{N}{m}$). The flexure stiffness was optimized in FEA, then tested using an Instron machine after manufacturing to account for error due to manufacturing tolerances.

3.2.2 Sensors and Control

The position of the stage and therefore the sample, was measured in the x and y axis using Renshaw encoders with an accuracy of 30nm and resolution of 1nm, and saved in Labview. A schematic of the Labview control for the voice coil actuator is shown in Figure 3.6:

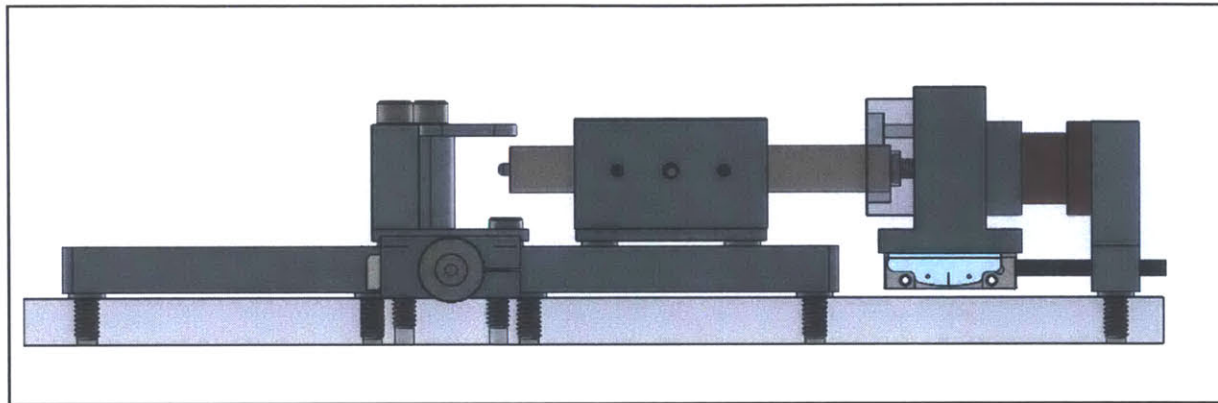


FIG 3.5: Side view, Renshaw linear encoder for x axis positioned on bottom surface of voice coil shaft mounting block.

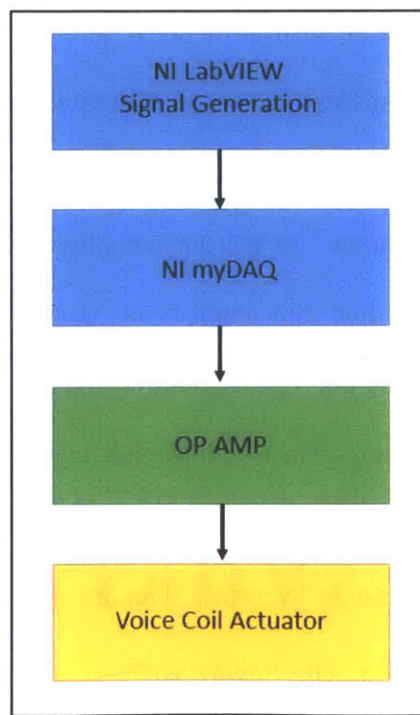


FIG 3.6: Voice Coil Actuation with Labview Control

The scaling value to convert current load to force was specified by the manufacturer and validated through calibration - measuring the force output for a series of input currents.

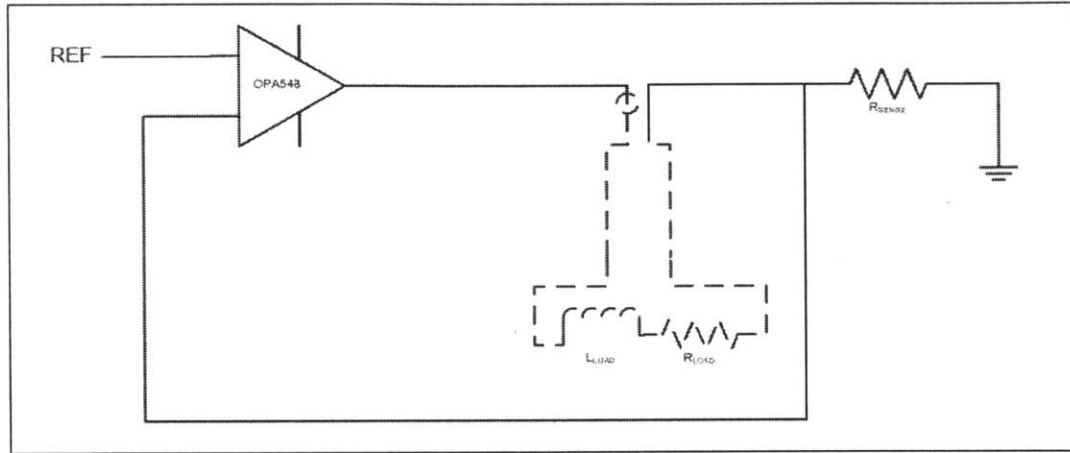


FIG 3.7: Current Control schematic for VCA operation

$$F_{output} = I_{load}(3.75N/A) \quad (11)$$

The Labview controller supplied a reference voltage, set by the user. The relationship between output force and the input voltage is represented by Equation 13.

$$I_{load} = \frac{V_{ref}}{R_{sense}} \quad (12)$$

$$F_{output} = \frac{V_{ref}}{R_{sense}}(3.75N/A) \quad (13)$$

The voice coil actuator was controlled with a ramp function, which increased the force at a rate of 0.083N/s for test 1. For test 2, a single force value between one and five Newtons was set, and kept constant throughout the test. The schematic for the op amp board can be found in Appendix A.

3.3 Error Model and Uncertainty

To accurately analyze the data collected by the material property testing setup the total error of the system must be characterized. Table 9 summarizes the sources of error and their magnitude:

Table 9: Error Sources for Material Testing Setup

Error Source	Affected Variable	X	Y	Z	Unit
Platform Flatness	-	0	0	8.2e-8	[m]
Thermal Expansion	δ , y, x	2.5e-6	2.4e-6	2e-7	[m]
Flexure Off Axis Travel	-	1e-7	0	0	[m]
δ Input Error (y)	δ	-	5e-7	-	[m]
Encoder error	y, x	3e-10	3e-10	-	[m]
VCA Force Error	F	0.002	-	-	[N]

Platform Flatness error is a function of the purchased aluminum baseplate manufacturing process. As the error is in the z axis, it does not affect the data.

Thermal Expansion error was calculated using the thermal expansion coefficient and an expected worst case temperature change of one degree Celsius along the load or displacement path.

Flexure Off Axis Travel is the distance travelled in constrained degree of freedom axes under the force required to displace the flexure the required travel distance. Only applicable to shear stiffness test.

δ Input Error (y) the error in micrometer positioning. Only applicable to shear stiffness test.

Encoder Error is the accuracy of the Renshaw encoders selected for displacement measurement on each axis.

VCA Force Error is a function of the accuracy of the current to force conversion value, the actual resistance of R_{sense} , and the real value of the reference voltage.

3.4 Functional Requirements Revisited

The functional requirements for the setup are revisited and compared with the actual values of the designed setup in Table 10:

Table 10: Functional Requirements Revisited

Property	Required Metric	<i>Designed Metric</i>	Units
Force Control	+/- 0.05	+/-0.02	N
Dimensional Stability	<1	2.6	μm
Displacement Resolution	<100	30	nm
Strain Rate	Constant +/- 0.5	<i>Constant +/- 0.1</i>	mm/s

The dimensional stability requirement was not met due to thermal expansion. The setup needs to be thermally stable within the entire timeframe of the test (approximately one minute). A thermal regulation box was constructed and placed around the setup during testing in order to minimize the effects of temperature fluctuations in the room on the position measurements.

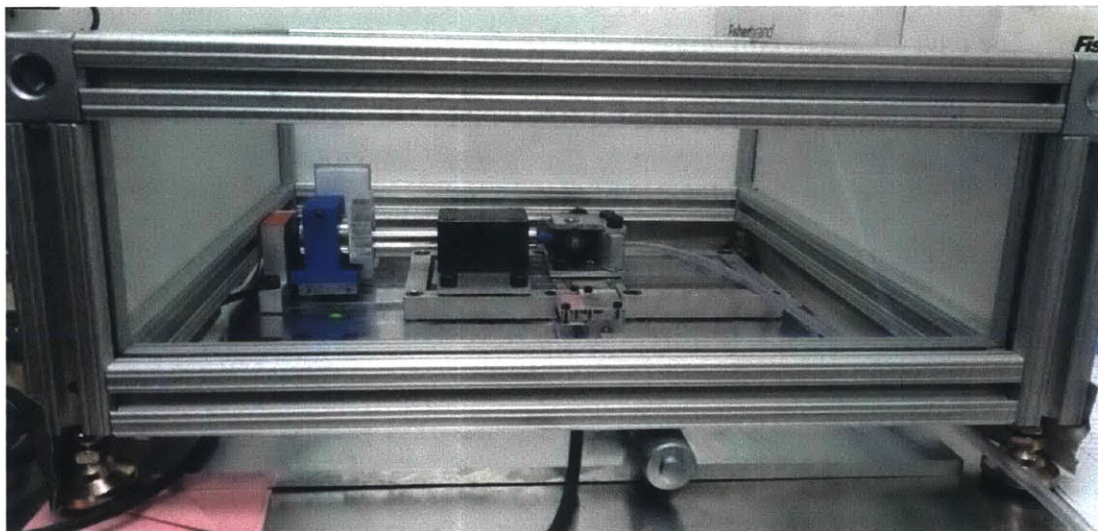


FIG 3.8: Thermal Regulation box surrounding the setup

EXPERIMENTAL DESIGN AND RESULTS

Section 4.1 outlines the sample preparation process, while Sections 4.2 and 4.3 detail the respective procedures for shear and axial stiffness testing. In Section 4.4 the results are summarized and discussed. In Section 4.5 the results are compared to those values found in the literature, and the magnitude of the shear and axial stiffness compared.

4.1 Preparation of Mice

The type CX3CR1-GFP mice used in testing were provided by MGH. Their mass ranged from 24.1-35 grams and age ranged from 10-14 months. All testing was performed in accordance with CAC protocols, and testing was performed exclusively with mice post-mortem. In order to fix the mouse skull to the setup, the skin was removed from the top of the skull, and the skull fixed directly to the plate with dental cement.

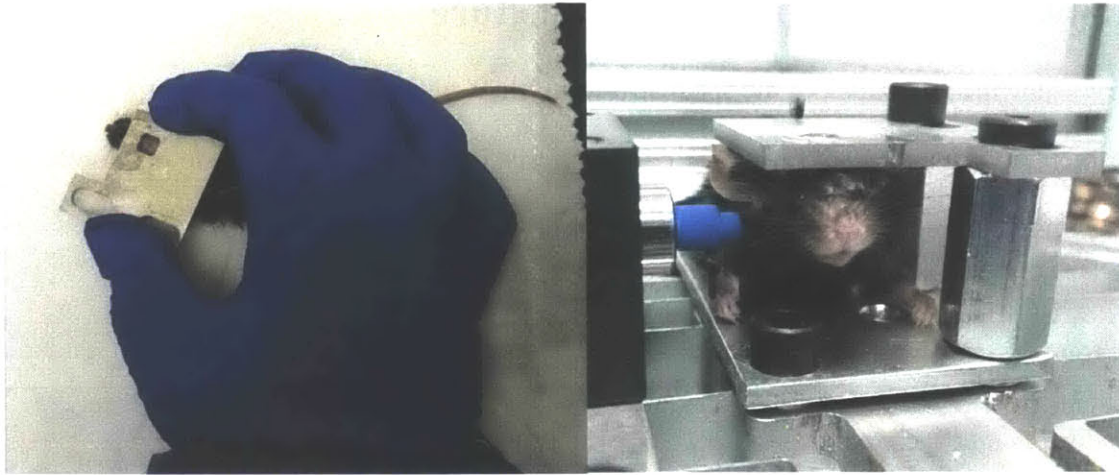


FIG 4.1: (a) Setup plate being glued to mouse skull (b) Mouse in setup with this fixation method

This attachment method was not strong enough, and so the fixation method was changed to include a screw drilled into the skull, with adhesive added around, as shown in Figure 4.2. This final method was used for all shear stiffness trials, as the interface between the skin and the bone is critical. For axial stiffness trials, the tissue of interest (skin, muscle) was removed, placed against an aluminum block in the setup, and tested. This was to remove the error due to torque around the central head attachment piece in the displacement readings.


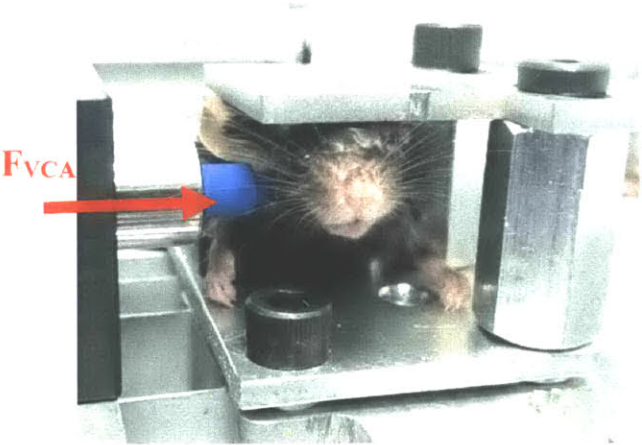


Figure 4.2: Screw and dental cement attachment

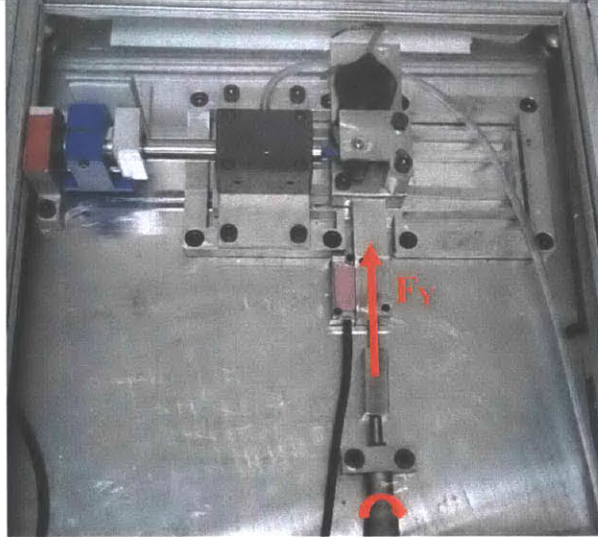
4.2 Shear Stiffness Testing Procedure

To determine the magnitude of the shear stiffness, which in this case includes the frictional force, experimental testing was performed. A constant force of 5N was applied in the direction normal to the skin to compress the tissue in a manner similar to the proposed constraint method.

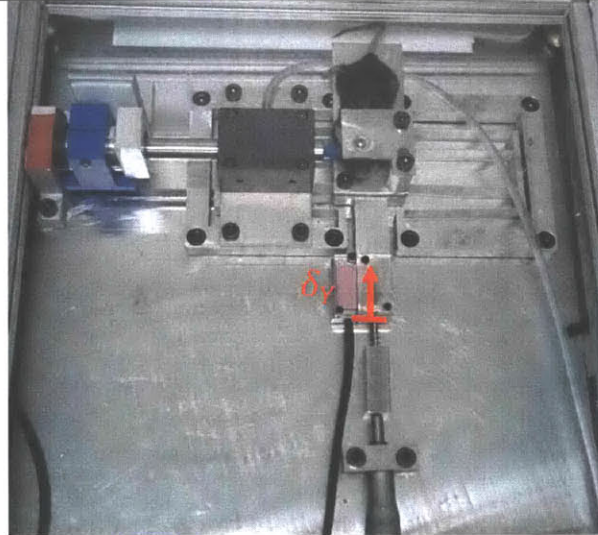
The Protocol is outlined below:

1) Place mouse in setup and adjust height such that VCA probe is between the eye and ear.	
2) Apply specified constant force to mouse skull with VCA	

3) Apply Force to mouse in y by moving micrometer a specified distance and therefore compressing spring



4) Record Position Data for y displacement



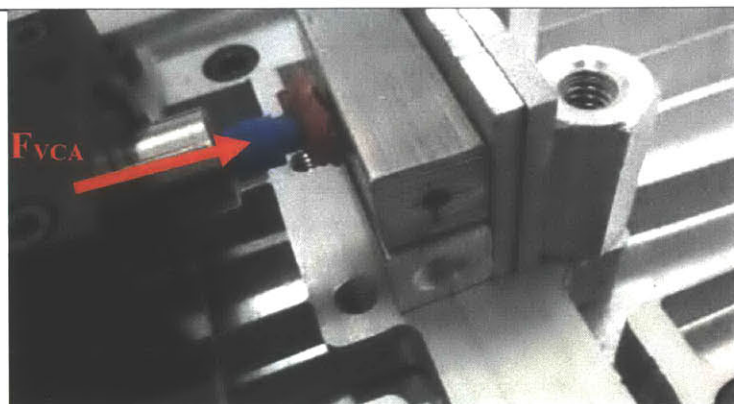
4.3 Young's Modulus (Axial Stiffness) Testing Procedure

Skin is a nonlinear elastic material, therefore the stiffness of the skin varies as a function of strain. To find the shape of this stiffness curve, the displacement as a function of input force will be measured for the tissue as a whole and for independent sections of the tissue. The material property setup was used to test the stiffness of the skin and muscle layers separately. These samples were taken from the cheek of each mouse. The protocol is outlined below.

1. Place tissue of interest in setup against aluminum block. The threshold force for thickness measurements and determining point at which the contact is touching is 0.01N.



2. Apply Ramp Force with Voice Coil at rate of 0.083N/s. Measure displacement of voice coil in x axis using Renshaw encoders.



Additional axial stiffness data for tissue samples was collected using an Instron machine, as pictured in Figures 4.3 and 4.4. Samples were prepared by punching a 6mm diameter piece from the excised material. The threshold force used to determine when the instron plate engaged with the tissue and measure the tissue thickness was 0.01N.

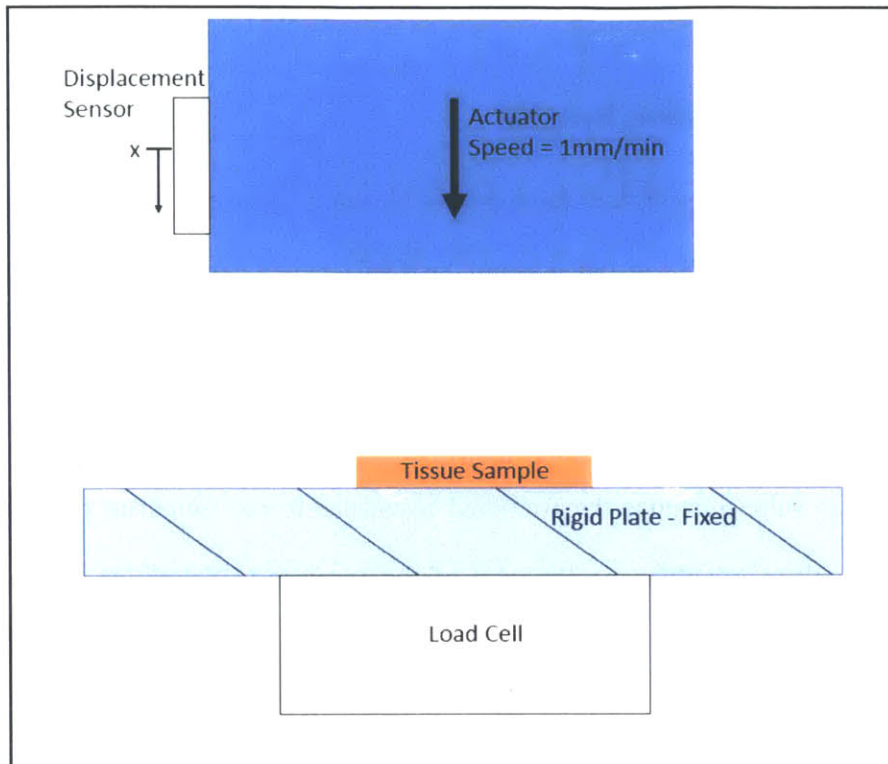


FIG 4.3: Instron setup schematic

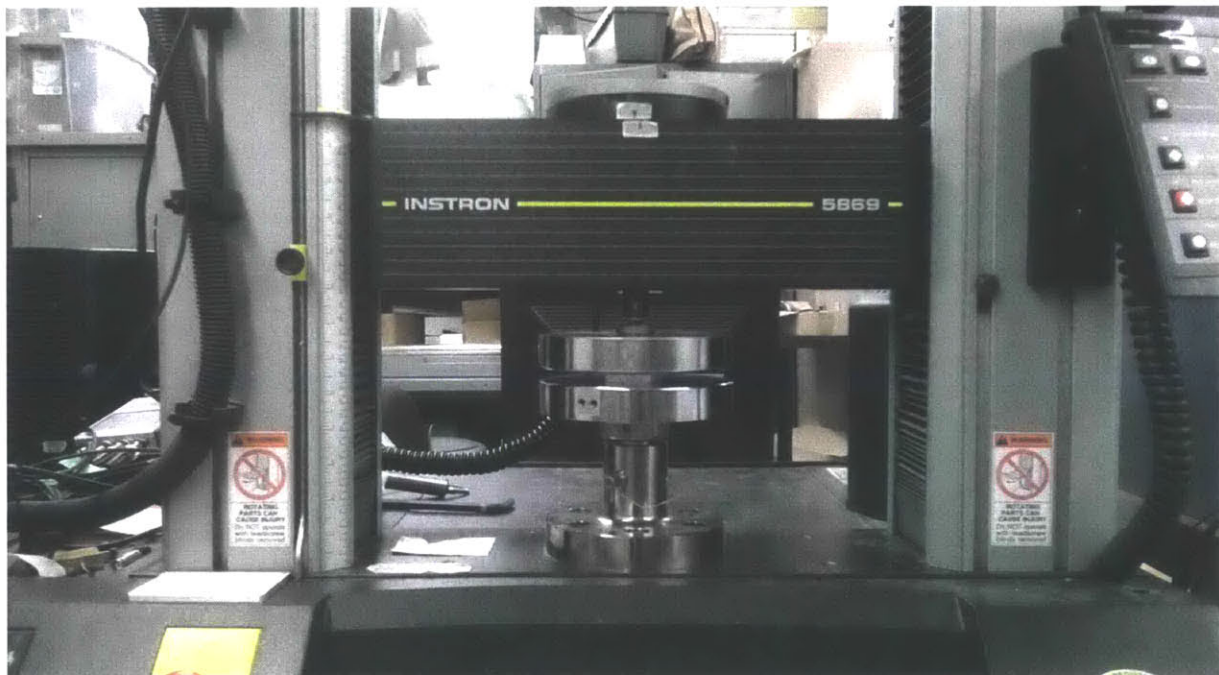


Figure 4.4: Instron testing setup

4.4 Results

4.4.1 Shear Stiffness Testing Results

Tests were conducted with the constant force of five Newtons applied to the skin in the x axis. The push spring was then displaced a distance δ , and the displacement y of the mouse measured. These values were used to find the shear stiffness of the skin.

$$k_{shear} = \frac{k_{spring}(\delta - y) - k_{flexure}y}{y} \quad (14)$$

This shear stiffness value includes the frictional resistance to movement in that axis, which is variable and difficult to quantify. As the goal of the test was to determine whether the shear resistance (a combination of shear stiffness and friction) was significant compared to the axial stiffness, it was not necessary to find each value separately. Figure 4.5 shows the calculated shear stiffness value at each input displacement, plotted for the measured values, and the minimum and maximum effect of the system error.

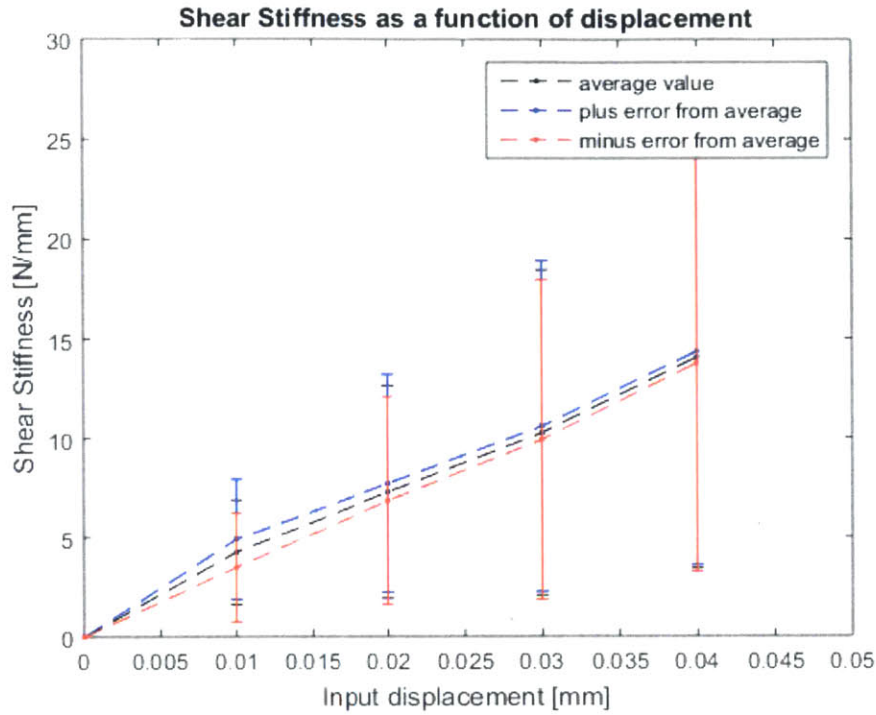


FIG 4.5: Shear Stiffness as a function of input displacement. The error bars represent one standard deviation from the mean. The system error (represented by the three separate lines) is small compared to the variation between trials.

As expected, the stiffness increases as displacement increases, reflecting the fact that as the skin is pulled taught it becomes more difficult to pull it further. The relatively large variation in measured values could be a result of the ‘stick/slip’ phenomenon, where for certain trials the static friction was overcome and the probe slid against the tissue, while for others slipping never occurred and the skin itself was stretched. The values are summarized in Table 11.

Table 11: Shear Stiffness Values

Input Displacement δ (mm)	Average Measured Displacement x (mm)	Average Shear Stiffness (N/mm)	Standard Deviation (N/mm)
0	0	0	0
0.01	0.0050	4.2	2.9
0.02	0.0086	7.3	5.4
0.03	0.0113	10	8.2
0.04	0.0130	14	11

4.4.2 Axial Stiffness Testing Results

The Young's Modulus was characterized for skin samples and muscle samples taken from each cheek (one of the proposed contact locations) of the sample mice. Each of the force-displacement curves was fit using Equation 15, where $F_T = 0.01\text{N}$ is the threshold force, and d is the displacement of the tissue:

$$F = F_T(e^{pd} - 1) \tag{15}$$

There was good agreement between the experimental data and the curve fitting equation. Example test results are plotted in Figure 4.6 against Equation 15 with a p value of 35.

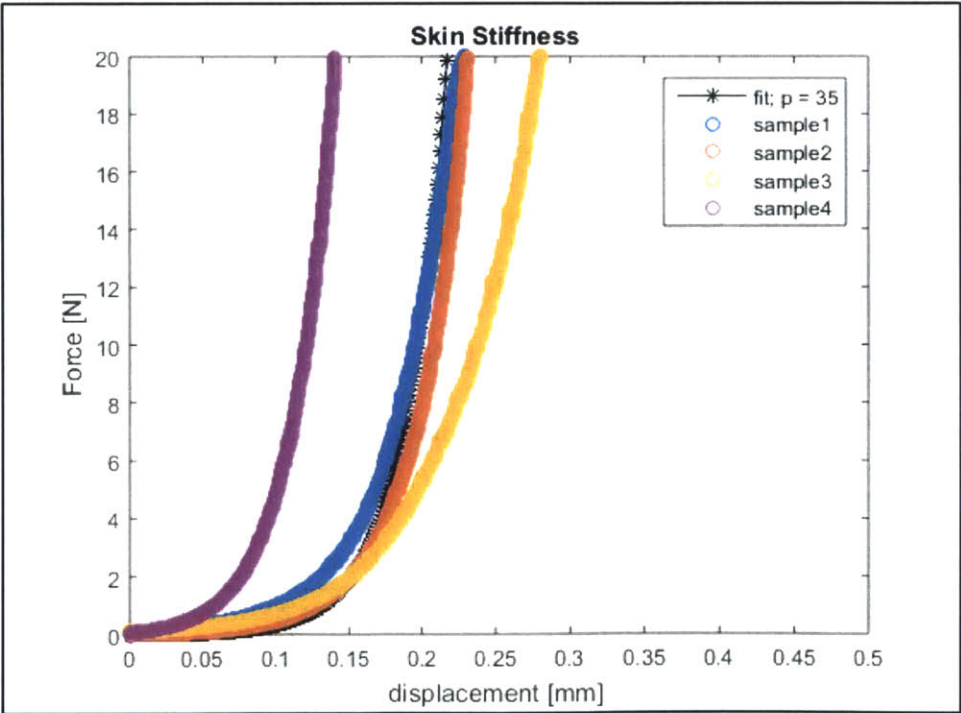


FIG 4.6: Raw data from multiple skin trials plotted against curve fitting equation of $p = 35$

The average and standard deviation for all samples (n=12) are summarized in Table 12:

Table 12: Measured Material Properties

Parameter	Skin (cheek)	Muscle (cheek)
Average thickness (mm)	0.455	1.03
Thickness Standard Deviation (mm)	0.063	0.38
Average q value	11.49	7.85
q value standard deviation	0.141	2.50
Average p value	25.50	7.70
p value standard deviation	3.535	0.42

4.5 Discussion and Comparison to Values from Literature

The modulus and thickness values measured for mouse skin agree with those values found in the literature. For muscle, there is no published data available specifically for mouse muscle layers on the head, but the data collected for the modulus coefficient is in the range of that measured in human muscle using other methods. Table 13 contains a summary of the values found in the literature and the values measured in the tests.

Table 13: Material Property Values

Tissue Type	q Value Range	Thickness Range (μm)	Source
Mouse skin (Face)	11.49 ± 0.14	455 ± 63	Testing Chp 3-4
Mouse skin (Hind Limb)	--	211 - 671	[1]
Mouse skin (Hind Limb)	10.77 ± 2.03	278 ± 102	[20]
Mouse Muscle (Face)	7.85 ± 2.50	1030 ± 380	Testing Chp 3-4
Bovine Muscle	5.5	--	[22]
Rabbit Muscle (Soleus)	4.6 - 7.4	--	[23]

The values for skin thickness and young's modulus measured by Wang et al [1] [20] were taken from mice varying in age, hair cycle, body weight, and skin site. The skin samples tested were taken from the distal and proximal ends of the hind limb as well as the saphenous nerve trunk. Wang et al. concluded that stiffness varied inversely with thickness, but this effect resulted in a consistent modulus (represented by coefficient q) across hair cycle stages and body weights. The

modulus of skin from different anatomical locations varied significantly, with skin containing structures such as nerves and blood vessels having a higher modulus. Therefore, at a given skin site, the elastic compression modulus remains consistent throughout a mouse's life.

The ranges for moduli and thickness listed in this table will be used to characterize the possible performance of a constraint system that interfaces with the tissue in Chapter 5. To determine whether or not the shear stiffness is significant when compared to the axial stiffness, the two values must be compared. In order to find the axial stiffness from the q values in the literature, the modulus coefficient q may be related to the stiffness coefficient p by the section thickness, t_0 .

$$p = \frac{q}{t_0} \quad (16)$$

For the values of q and t_0 found in the literature and verified by testing, a p value range of 17-72 was found. Using the mean values measured in Chapter 4 of $q = 11.49$ and $t_0 = 455$, which also fall within the published ranges, a p value of 25.25 was calculated. Plotting the stiffness curve for $p = 25.25$, the mean value for facial skin and at the lower end of the stiffness range, and taking the slope for a displacement of $10\mu\text{m}$ around $F = 5\text{N}$, the projected mean for contact force, we find:

$$k_{axial} = 141.01 \text{ N/mm} \quad (17)$$

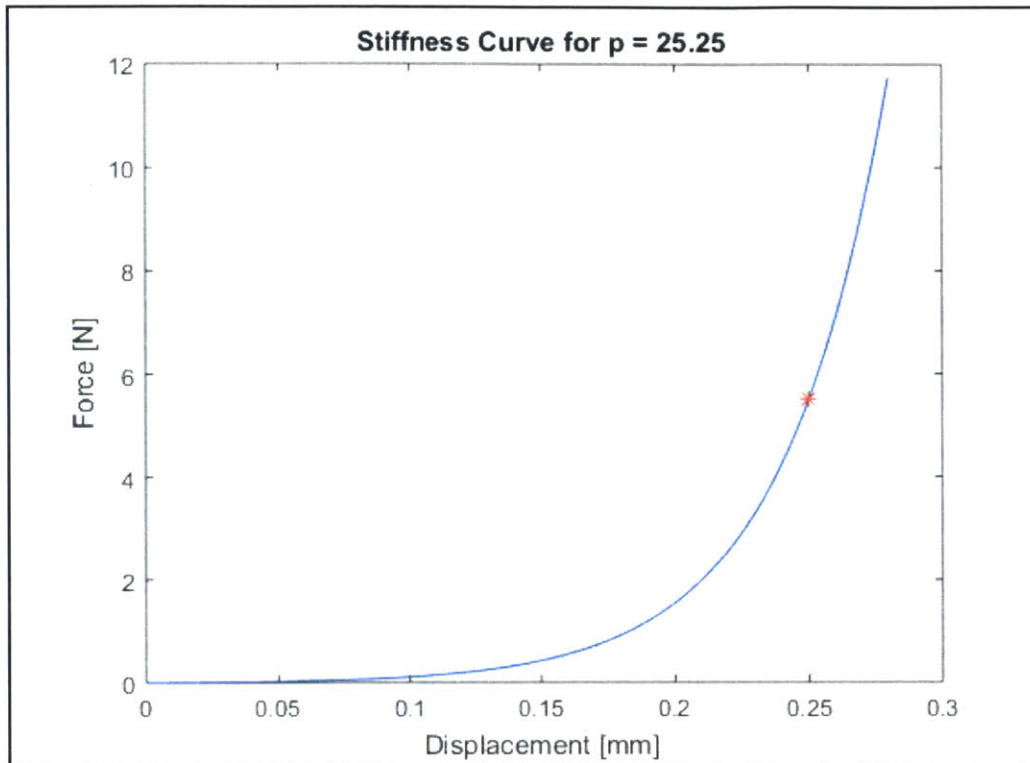


FIG 4.7: Stiffness curve for $p = 25.25$, with red dot representing point around which Young's Modulus was linearized with step size of $10\mu\text{m}$

In Section 4.4.1 the shear stiffness for the first $10\mu\text{m}$ of travel under a 5N contact force had a mean value of 4.27 N/mm, two orders of magnitude less than the axial stiffness (141 N/mm) on the lower end of the spectrum. Therefore the shear stiffness and frictional force will be neglected, such that each contact is considered to provide constraint to the system in only the axial direction.

PREDICTING CONSTRAINT SYSTEM PERFORMANCE

The material property values found and outlined in Chapters 2-4 may be used to predict the performance of the system as a function of the applied contact force and number of constraints. This Chapter will outline the general procedure for predicting the error, or internal displacement of a rigid body surrounded by a deformable layer.

5.1 System Behavior

The mass spring model and force inputs for the system are demonstrated by the model in Figure 5.1. First a contact force F_a is applied, compressing the tissue and increasing its stiffness to some value k_{tissue} . Then, the mouse applies a force F_{mouse} in an attempt to escape the restraint, resulting in a displacement δ of the rigid bone layer from its initial position.

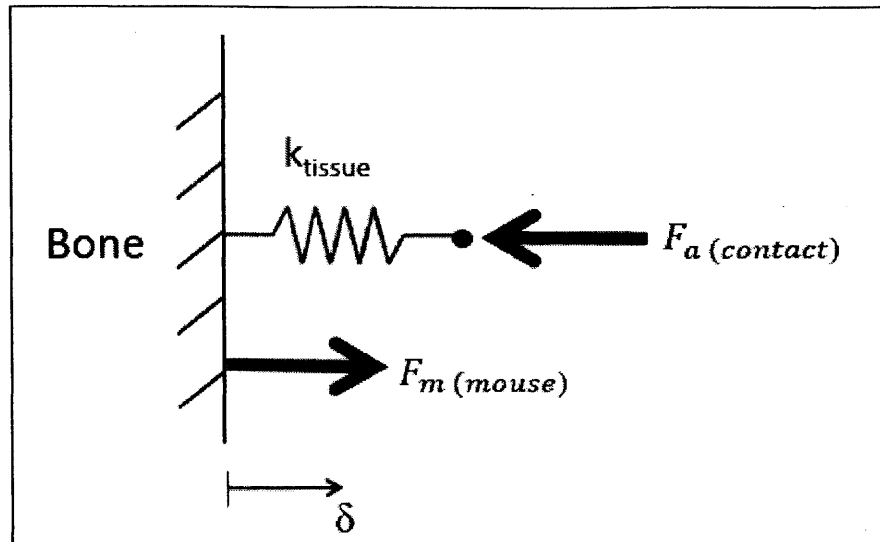


FIG 5.1: Spring model and Force inputs for derivation of mouse position error, δ .

The error is represented by δ , the motion of the bone (equivalent to the skull, our imaging area of interest in the mouse restraint case). Using the nonlinear curve fit (Equation 3 in Chapter 2) to describe the change in modulus E as a function of strain, the value of δ may be found. The parameters used in the model and following equations are listed below:

F_a = Contact Force [N] – force applied by the restraint device

F_m = Mouse Force [N] - force applied by the mouse attempting to escape

F_T = Threshold Force [N] - force at which resistance is felt during materials testing

q = Modulus Coefficient [-] - Coefficient to describe the shape of the nonlinear stiffness curve

t_0 = Initial Thickness [m] - Initial thickness of the deformable layer

E = Young's Modulus [N/m^2] - Material Property describing stiffness

A = Contact Area [m^2] - area of contact of restraint device

ϵ = Strain [-] - normalized displacement (change in thickness/initial thickness)

σ = Stress [N/m^2] – local stress applied by each contact

The threshold force, $F_T = 0.01\text{N}$ is the change in force from zero during a force vs displacement test that signifies contact has been made with the material. The threshold stress is the stress corresponding to the threshold force;

$$\sigma_t = \frac{F_T}{A} \quad (18)$$

The initial modulus E_0 may be found by multiplying the threshold stress by the modulus coefficient

$$E_0 = \sigma_T q \quad (19)$$

The general equation representing the nonlinear modulus of the curve;

$$\sigma = \sigma_T (e^{q\varepsilon} - 1) \quad (20)$$

can be solved for the strain, ε ;

$$\varepsilon = \frac{1}{q} \ln\left(\frac{F_T + F_d}{F_T}\right) \quad (21)$$

which is by definition also equal to;

$$\varepsilon = 1 - \frac{d}{t_0} = \frac{\delta}{t_0} \quad (22)$$

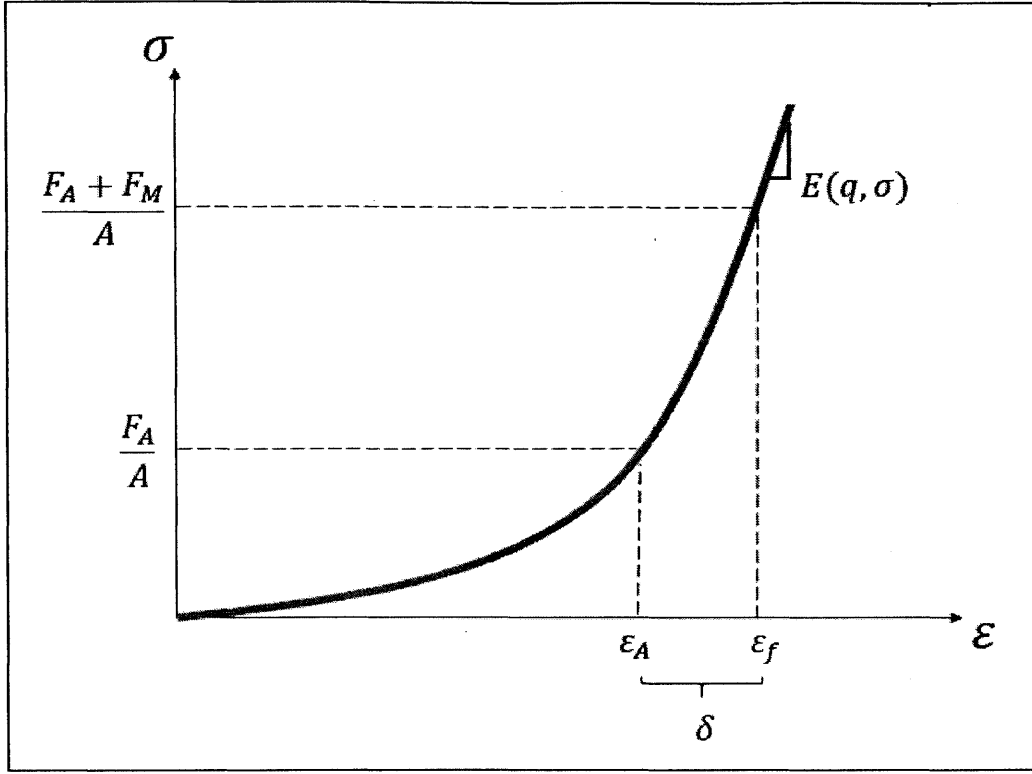


FIG 5.2: Nonlinear stiffness curve, with strain ϵ_A due to contact force and final strain ϵ_f shown. The Young's Modulus E may be calculated for a given strain by taking the slope of the line around that point.

For the mouse model, the position error $\delta = \Delta t$ is represented by the change in strain from the initial position ϵ_A reached due to contact force F_A , to the final position ϵ_f as a result of the mouse force F_M .

$$\delta = t_0(\epsilon_f - \epsilon_A) \quad (23)$$

Solving for ϵ_A and ϵ_f ;

$$\epsilon_f = \frac{1}{q} \ln\left(\frac{F_M + F_A + F_T}{F_T}\right) \quad (24)$$

$$\epsilon_A = \frac{1}{q} \ln\left(\frac{F_A + F_T}{F_T}\right) \quad (25)$$

Substituting in equations 22, 24, and 25, Equation 23 may be rewritten:

$$\delta = \frac{t_0}{q} \ln\left(\frac{F_M}{F_A + F_T} + 1\right) \quad (26)$$

Equation 26 may now be used to determine the performance of a constraint system, characterized by position error. This equation is only applicable to displacement and forces acting along the same axis. If multiple contacts are acting on that axis, the system stiffness will increase and the system error will decrease as a function of the number of contacts and their respective forces.

5.2 Dimensional Analysis

The Buckingham pi theorem states that an equation may be rewritten in terms of a set of $p=n-k$ dimensionless parameters $\pi_1, \pi_2, \dots, \pi_p$ constructed from the original variables, where n is the number of physical variables. Equation 26 derived in Section 5.1.1 to describe the position error of the system may be represented by three nondimensional variables.

$$\delta = \frac{t_0}{q} \ln\left(\frac{F_M}{F_A + F_T} + 1\right) \quad (26)$$

$$n = 5$$

$$k = 2$$

$$p = n - k = 3$$

Since $F_T = 0.01 \ll F_A, F_M$ it may be neglected, and the $n = 5$ variables are F_A, F_M, t_0, q, δ . The $k = 2$ parameters are Newtons and meters. The first pi group describes the force ratios

$$\pi_1 = F_m F_a^a t_0^{cb}$$

$$[m^0 N^0] = [N N^a m^b]$$

$$\pi_1 = \frac{F_M}{F_A}$$

The second pi group describes the relationship between the error, δ and the other variables

$$\pi_2 = \delta F_m^a F_a^b t_0^c$$

$$[m^0 N^0] = [N N^a N^b m^c]$$

$$\pi_2 = \frac{\delta}{t_0} = \varepsilon$$

The final pi group is just the non-dimensional variable q that describes the shape of the curve

$$\pi_3 = q$$

These relationships describe the worst case performance of the constraint system, which occurs when the mouse applied the maximum force it is capable of, described by F_M . This worst case occurs when the mouse applies the maximum force it is able to. It is expected that for the majority of the imaging session, the performance of the system will be better than this worst case value, but this will be dependent on the behavior of the mouse. Conditioning of the animal may help to decrease how often the mouse attempts to escape and therefore applies a great deal of force to the constraints. How the worst case performance changes with the modulus coefficient and the force ratio is shown in Figure 5.3. The modulus coefficient π_3 and *Fratio* π_1 were selected for the ranges relevant to the mouse restraint case. The best performance occurs at the bottom right corner of the graph, as q increases and the force ratio decreases.

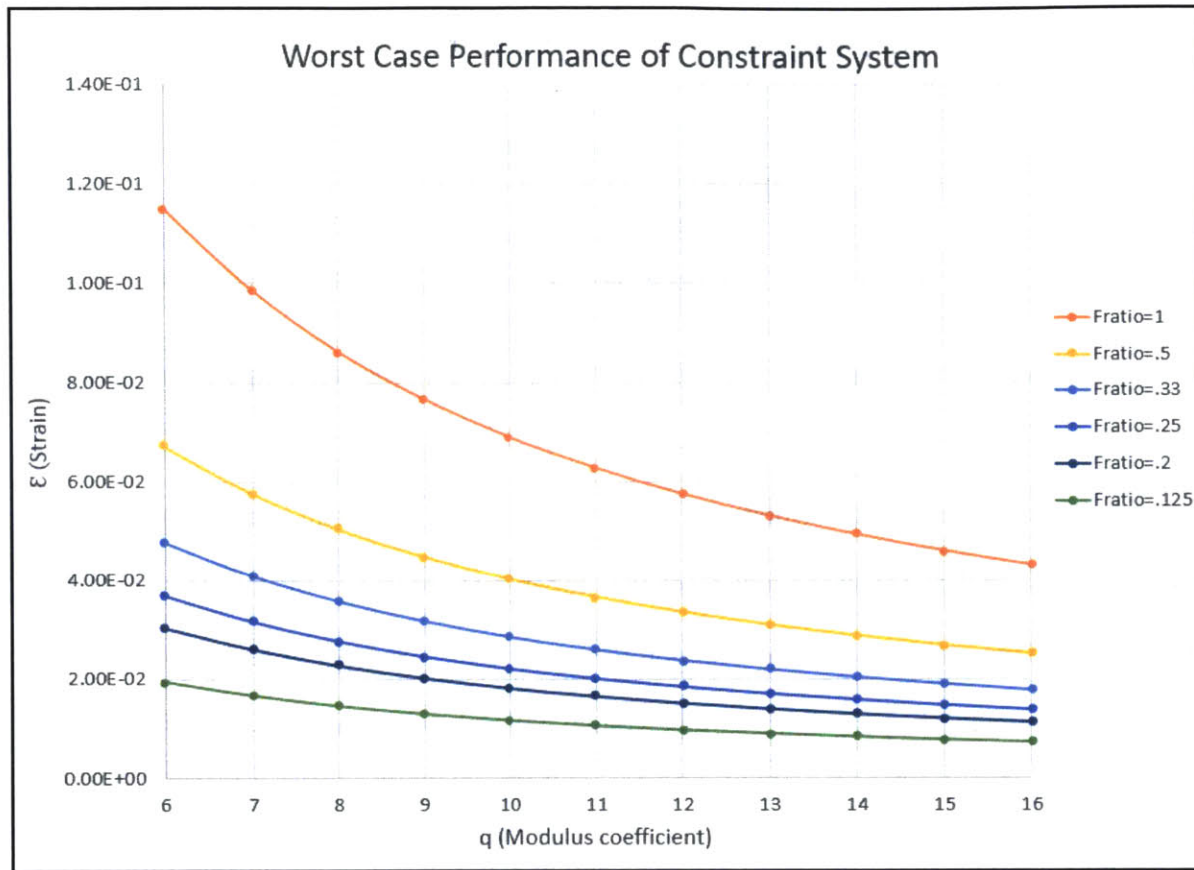


FIG 5.3: Graph of non-dimensional parameters $\pi_3(q)$ vs $\pi_2(\epsilon)$ as a function of $\pi_1(Fratio)$ to demonstrate worst case performance

In order to find the actual error of a given system – defined as the displacement that occurs in each axis when the mouse applies its maximum force there are two additional steps. First, the total force in each axis must be calculated by summing the components of every contact that are normal to a given axis. Second, the strain must be divided by the initial tissue thickness in order to calculate the displacement. Using the above theory, the worst case performance range may be determined for the mouse restraint system. In this specific application, the contact force F_A , is limited by the bone thickness and geometry of that location on the skull. The applied force F_M , is dependent on the mouse, but is estimated as worst case scenario maximum value.

5.3 Calculating Maximum Allowable Contact Force

To determine what the force ratio for a given constraint will be, it is necessary to determine the maximum allowable contact force at that skull location. In this section the approximation used for max contact force is outlined.

5.3.1 Bone Model and Failure Calculations

The maximum force that may be applied to each area of the skull was calculated assuming three point beam bending with the contact modeled as the central applied point load and the side reaction force coming from the point where the skull curves such that the bone is aligned axially (and is therefore much stiffer) with the contact load.

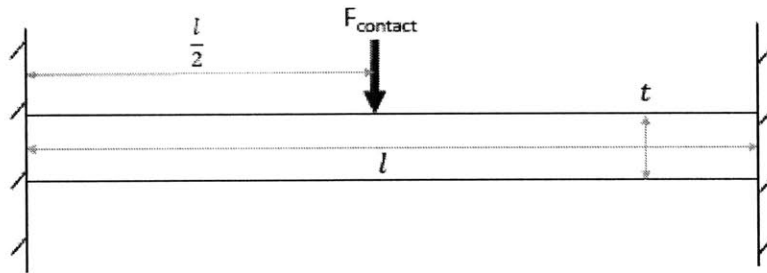


FIG 5.4: 3 point bending schematic, with each bone section modeled as a beam of length l , thickness t , width w .

To calculate the maximum force applied, we will consider the bending stress on the beam, and then use a safety factor of 1.5 to determine the maximum force based on the yield stress of bone. The bending stress $\sigma_{bending}$, is a function of the moment M , the distance from the neutral axis y , and the beam moment of inertia I .

$$\sigma_{bending} = \frac{My}{I} \quad (27)$$

$$I = \frac{wt^3}{12} \quad (28)$$

$$M = \frac{F_{contact}l}{8} \quad (29)$$

$$y = \frac{t}{2} \quad (30)$$

The yield stress of bone is [25]:

$$\sigma_{ys} = 104MPa - 121MPa$$

To be conservative, the minimum value of 104MPa will be used. With a safety factor of 1.5, the maximum allowable bending stress is:

$$\sigma_{max} = \frac{\sigma_{ys}}{1.5} = 69.3MPa \quad (31)$$

Then for each section of bone to which a contact force is applied, we may solve for the maximum allowable contact force F_{max} :

$$F_{max} = \frac{\sigma_{max}4wt^2}{3l} \quad (32)$$

5.3.2 Maximum Force Calculated for Each Area of the Skull

A laboratory mouse skull was obtained and the relevant measurements of bone thickness and critical dimensions taken using calipers. These values were used in the three point bending approximation outlined above to calculate the maximum allowable contact force at each proposed contact location, with a safety factor of 1.5. A model of the mouse skull is shown in Figure 5.5 with the proposed contact locations numbered. Table 14 lists the dimensions used and the maximum contact force calculated for each location.

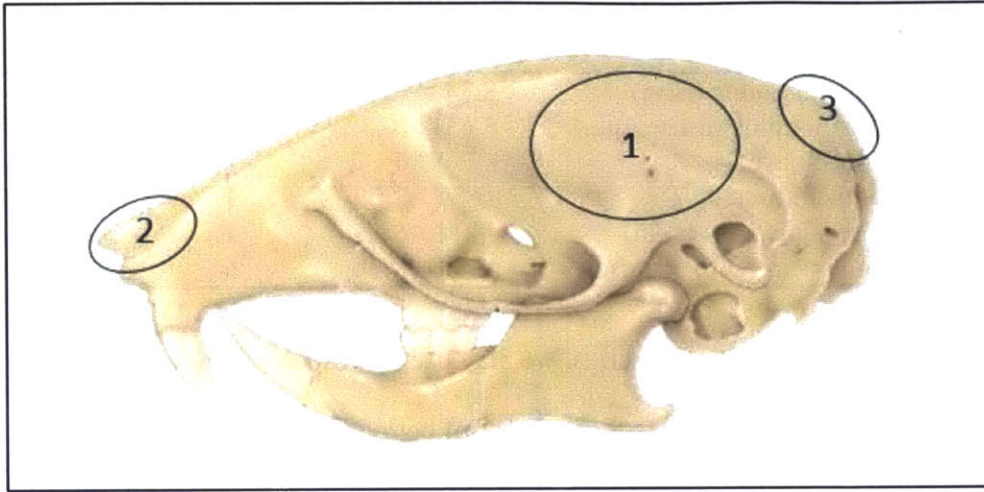


FIG 5.5: Mouse skull with proposed contact locations encircled and numbered

Table 14: Maximum Contact Force at Skull Locations

Skull Location	Number	Length [mm]	Bone Thickness [mm]	Max Force[N]
Eye/Ear Area	1	0.008	0.04	9.24
Top of Nose	2	0.008	0.04	11.1
Back of Head	3	0.01	0.04	5.91

These force values will be used to predict the performance of the device in Chapter 7.

5.4 Discussion of Expected Performance Range

Based on the known values of q and the maximum contact force for each location, it is possible to determine the worst case performance in each axis. The known ranges for each value are shown in Table 15, and the worst case performance (expected error) is calculated for the worst case δ_w (minimum thickness, maximum q , maximum F_A) and best case δ_b (maximum thickness, minimum q , minimum F_A) of the material property range. The skin and muscle modulus are treated as separate springs, and the displacement for each will be found.

Table 15: Input Ranges for Prediction of Performance

Property	Range	Symbol	Units
Mouse Tissue modulus (skin)	8.74 – 12.80	q_s	---
Mouse Tissue modulus (muscle)	5.65 – 10.32	q_m	---
Mouse Force	1.96	F_M	N
Contact Force	3.77 – 7.02	F_A	N
Mouse Tissue Thickness (skin)	211 - 671	$t_{0,s}$	μm
Mouse Tissue Thickness (skin + muscle)	650 - 1430	$t_{0,m}$	μm

As the muscle and skin are springs in series, we may use the respective values of t_0 and q to find a value for p equivalent that represents the stiffness of both layers.

$$p_{eq} = \left(\frac{t_{0,s}}{q_s} + \frac{t_{0,m}}{q_m} \right)^{-1} \quad (33)$$

Then, the limits of the ranges for tissue thickness and modulus may be substituted into Equation 33 to find the best and worst case values for p_{eq} , which may then be used to find the best and worst case displacement:

$$\delta_b = \frac{1}{p_{eq,b}} \ln \left(\frac{F_M}{F_A + F_T} + 1 \right) = 23 \mu m \quad (34)$$

$$\delta_w = \frac{1}{p_{eq,w}} \ln \left(\frac{F_M}{F_A + F_T} + 1 \right) = 129 \mu m \quad (35)$$

These results suggest that in order for this approach to restrain an awake mouse to less than a micron of movement in a single axis, the contact force would either need to be increased to over 100N, or at least 23 separate contacts (assuming ideal tissue parameters and maximum contact force) must be implemented in each axis. Neither of these approaches are possible, as the first would kill the mouse, and the second is not feasible given the space constraints. As a result, the focus for the device will be improved performance for the restraint of anesthetized mice.

5.4.1 Performance for Anesthetized Mouse Case

In the case of an anesthetized mouse, the performance of the system should be significantly better than for an awake mouse. The force applied by the mouse will only be that due to normal respiration, heart beat and involuntary convulsions. This force is estimated to be significantly less than the maximum force from the mouse's attempts to escape. While a satisfactory way to estimate this force has not been found, the device will be tested experimentally on an anesthetized mouse and the performance measured.

DESIGN OF RESTRAINT DEVICE

This Chapter will outline the design of the mouse restraint device based on the information detailed in previous chapters. Section 6.1 reviews the functional requirements first discussed in Chapter 1.3. Section 6.2 will discuss the specifics of applying kinematic constraint theory to a mouse head, and show the selected contact locations. Section 6.3 presents the mechanical design and use considerations.

6.1 Functional Requirements

The functional requirements for the restraint device were derived from discussions with researchers who use laboratory mice in their experiments. Their input in conjunction with the available imaging technology and structures of interest determined the necessary requirements for a device that not only restrains mice but is safe, follows CAC protocol, and is easy for the researcher to use. These requirements are outlined in Table 15.

Table 16: Restraint Device Functional Requirements

Metric	Required	Desired	Units
Slow Drift	10	2	% of image
Mouse Movement (x, y)	<1	<1	micron
Mouse Movement (z)	<0.7	<0.7	micron
Geometry	5x5	5x5	cm
Applied Force Accuracy	+/- 1	+/-0.5	N

6.2 Application of Kinematic Constraint Theory

Kinematic constraint is often used in mechanical design as it provides reliable positioning of an object using a minimal number of contacts[29]. By using one contact to constrain each degree of freedom, highly accurate and repeatable positioning is possible. However, one of the limits of kinematic constraint is the high stress induced at each contact point and the low system stiffness.

Elastic averaging is a method of constraint in which improved accuracy is derived from averaging areas over a large number of contacting surfaces. The solid body is over constrained by a large number of relatively compliant bodies, whose elastic properties allow for the size and position error of each feature to be averaged over all contacts during preloading. Although repeatability and accuracy are lower for an elastically averaged system than a kinematically constrained system, there is higher stiffness and lower local stress at each contact location.

6.2.1 Assumptions for Kinematic Constraint

Kinematic constraint theory was applied to the design of a mouse head restraint device in order to prevent movement in any degree of freedom. However, due to the unique structure of the mouse skull, there are limitations to the possible locations of contact points, and so more than six contacts were actually used to constraint all degrees of freedom. In order to apply kinematic constraint theory to the mouse skull several assumptions were made:

- 1) Every contact is a point contact. Although the contact area is larger than a point (diameter = 2mm), the surface roughness and uneven bone structure underneath the deformable tissue layer lead to the assumption that there is a single location at which the deformation is greatest, and this is the stiffest point (since stiffness increases with strain).

- 2) Shear Stiffness is negligible. This assumption follows from the results of material testing outlined in Chapters 3 and 4. As a result of this assumption, every contact provides constraint only in the normal direction of force application.
- 3) The contact is infinitely stiff compared to the tissue. The Young's Modulus for the contact material, Aluminum is on the order of 70GPa. In comparison, the Young's Modulus for biological tissue ranges from 3KPa to several MegaPascals. As several orders of magnitude separate the modulus values, the contact may be modeled as infinitely stiff.
- 4) A system degree of freedom is considered constrained when an equivalent rigid body subject to the same contact would be kinematically constrained. Although the reality of having low tissue stiffness means that there will be some deformation at the contact, and the rigid body inside will be able to move in the direction normal to the contact a displacement x that is a function of tissue stiffness, this assumption allows us to decouple the "error" due to tissue deformation from any error due to insufficient constraint of the body.
- 5) Contact Stiffness is negligible. For two bodies with relatively similar elastic moduli in contact, there occurs some deformation at the surface interface that may be modeled using Hertzian contact theory. As the stiffness of the system is dominated by the low stiffness of the skin layer, the contact stiffness can be neglected, as demonstrated in Chapter 2.3.2.

6.2.2 Geometry of Mouse Skull

The unique geometry of the mouse skull results in specific areas that need to be avoided in order to prevent injury or serious discomfort to the mouse. Figure 6.1 shows the areas to be

avoided, which were determined through discussion with research scientists at MGH who work with mice as test subjects on a daily basis, as well as criteria set by the Committee for Animal Care for protocol acceptance.

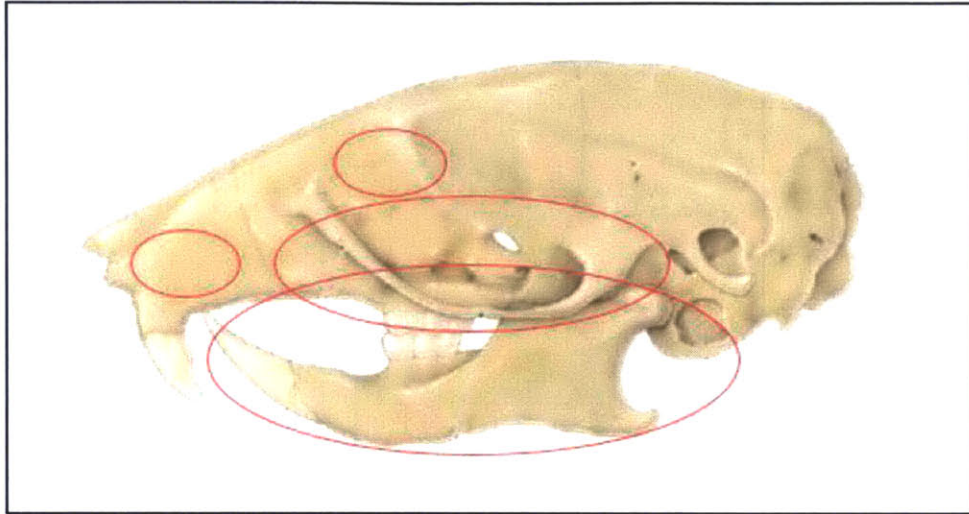


Fig 6.1: Areas to avoid contact on the mouse skull circled in red. These areas include the whiskers (due to sensitivity, to prevent discomfort in the mouse), the eye (to prevent injury), the cheekbone (it is too fragile to push with needed force), and the jaw (will not constraint the area of interest on the skull as the two pieces are not rigidly attached)

Laboratory mice come in a variety of shapes and sizes depending on their age, sex, and breed. The restraint device design must allow for the adjustment of each contact in x , y , and z in order to fit a range of head sizes.

6.2.3 Constraint Location Selection

In the case of a rigid body where a constraint may be placed anywhere, only six contacts are needed to constrain every degree of freedom, as shown in Figure 6.2:

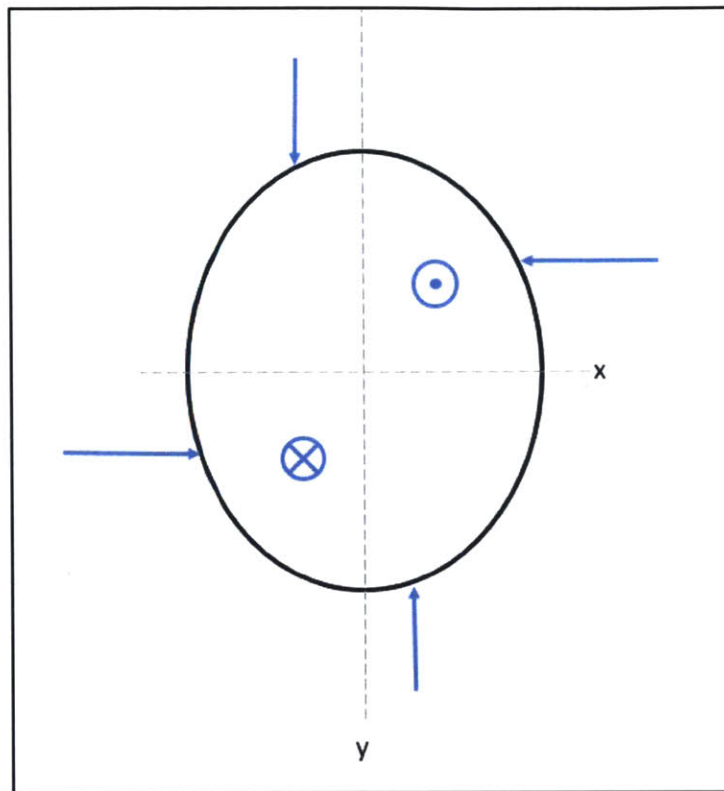


FIG 6.2: The six contact locations (shown in blue) needed to constrain all six rigid body degrees of freedom for the ellipsoid outlined in black.

To restrain the mouse skull, more than six contacts were needed. While ideally each contact serves as both a translational (negative or positive motion in an axis prevented) and rotational constraint (each rotational degree of freedom requires two contacts to be constrained, these contacts are ideally the translational constraint placed on opposite sides of the axis of rotation), in practice this was not possible. For the y axis constraint, it was only possible to place a contact exactly on the y axis itself at the nose location, so in order to constrain the θ_z degree of freedom two y axis contacts were used at the back of the head. Similarly, to constrain θ_y , two x axis contacts were used on each side of the skull, as the exact z location of the y axis is unknown. To constrain θ_x , three instead of two contacts were also used. In total, ten contacts were placed on the skull to restrain all six degrees of freedom.

6.3 Mechanical Design

This section will discuss the design of the restraint device shown in Figure 6.3.

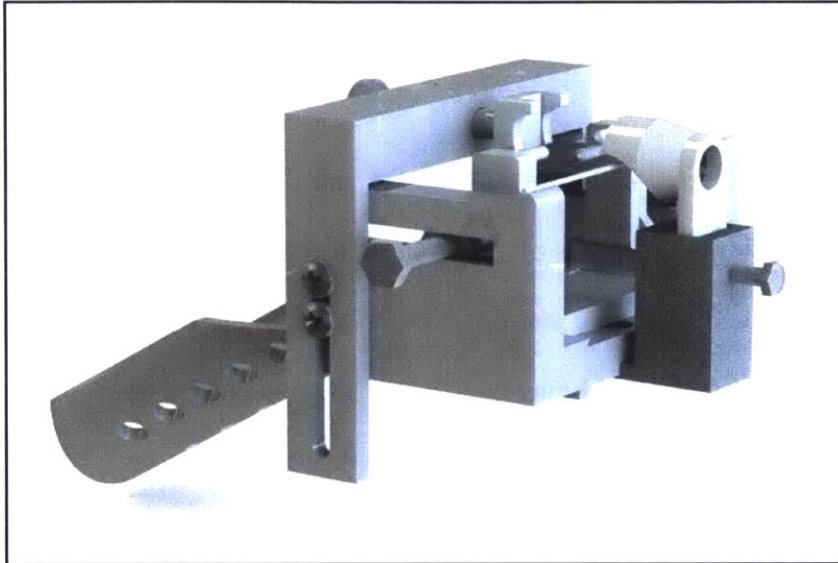


FIG 6.3: Restraint Device CAD

6.3.1 Use Case Considerations

The restraint device was designed to allow the mouse to be easily placed in the holder while anesthetized, then supplied with anesthetic while the constraint contacts are positioned and tightened to the desired force. The bite bar provides the reference for positioning the mouse when it is first placed in the holder, then each contact is adjusted to contact the appropriate point on the mouse's head. The snout constraint piece is the first piece put into place after the teeth are placed over the bite bar, as it includes a fitting for the anesthetic supply line. This ensures the mouse does not wake up before it is properly constrained.

The body holder, seen jutting out of the back of the device at an angle, has an open top, allowing a heating element to regulate body temperature to be wrapped around the mouse. This is

required any time a mouse is anesthetized in order to keep its body temperature in the correct range. This design also gives the researcher easy access to the mouse to check its respiration rate, which should be on the order of one breath per minute while anesthetized, and to test if the mouse is awake by using a foot pinch.

6.3.2 Design Overview

The restraint device is shown in Figures 6.3 and 6.4. Each contact was designed to be adjustable in order to fit multiple sizes of mouse head, and to vary the force applied. The bite bar (yellow) serves as a positioning tool and provides restraint in the z axis. The nose cone (green) holds the anesthetic supply line and may be adjusted in the y and z axes in order to provide the proper restraint force in these directions. The position of the side contacts (blue) may be adjusted in the y axis to line up with the area of the skull between the eye and the ear, where they are tightened against the skull using screws that push against the flexure arm of the blue piece. Once the mouse has been placed in the holder, the rear contact holder is adjusted in the z axis and tightened with machine screws. The rear contact (red) is then adjusted in the y axis in order to provide the proper restraint force in these directions.

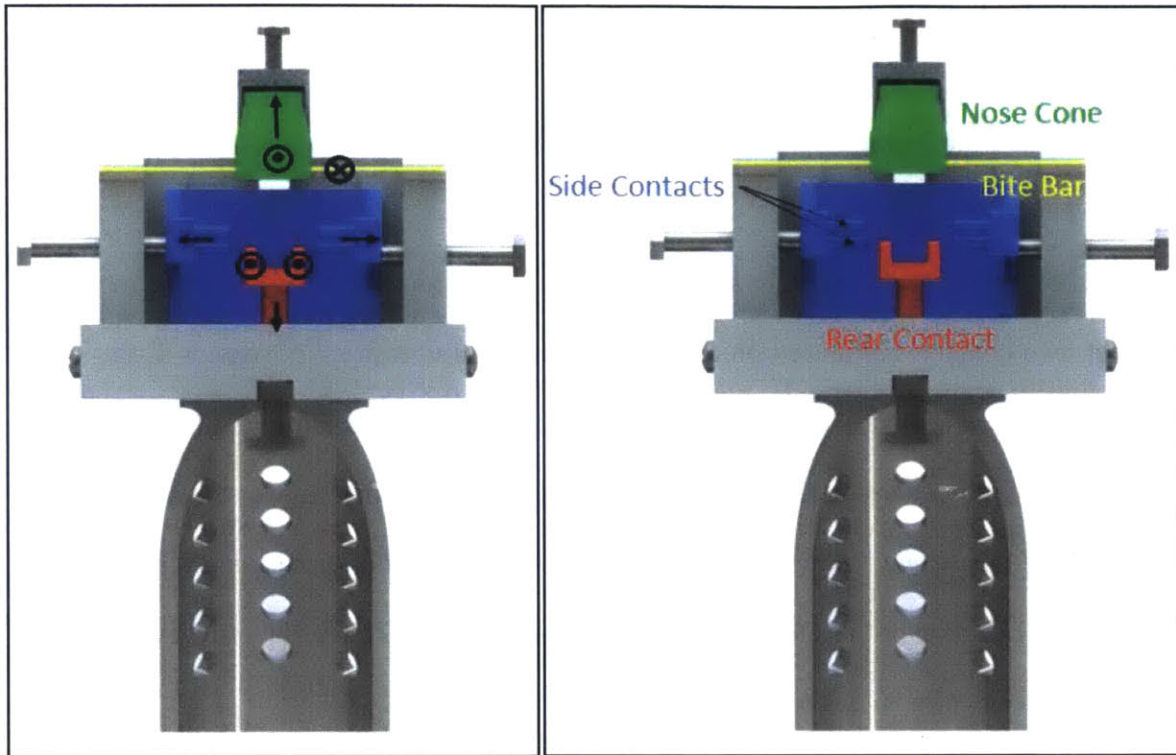


Figure 6.4: (a) Direction of constraint shown for each contact. (b) Top view of restraint device with contacts labelled.

The contact locations on the skull and the degrees of freedom constrained are shown in Figure 6.5:

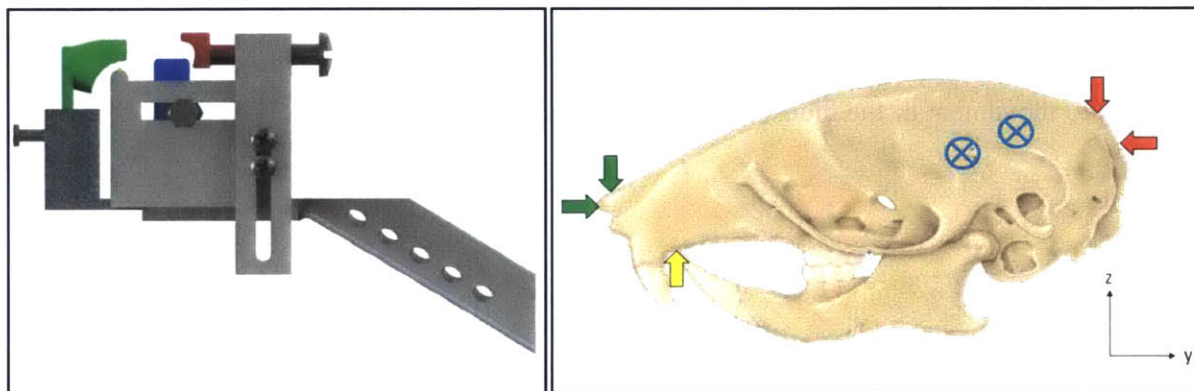


FIG 6.5: (a) Side view of restraint device (b) Side view of contact locations on skull with colors corresponding to contact pictured on device

A total of ten discrete contact points were used to constraint the skull. Due to the difficulty of accurately constraining a location far enough away from the axis of rotation, more than six contacts were needed. For example, the contacts restricting the rotation about the z axis are the two

blue contacts shown in Figure 6.5. A single contact would not suffice in this position because the location of the head's center of mass and therefore the z axis is unclear, and having only one contact on each side of the skull would not prevent rotation about z should the axis be located at the same y position as the contact.

This design differs from other stereotaxic device and from the 2012 prototype in several ways. First, two contacts are placed on each side of the skull to restrict movement in the x axis instead of one. These contacts are positioned on the flat of the skull instead of in the ear to reduce discomfort to the mouse. Second, the rear contact (red), and nose cone restrict the movement of the mouse in the y direction. Other devices rely on the shear stiffness of contacts placed along the sides of the skull and top of the snout to minimize y displacement. To test the efficacy of the rear contact, y displacement with and without the contact was tested.

The restraint device was 3D printed in ABS, and then assembled. Each of the force and location adjustment controls is a machine screw. The device was then attached to a Thor labs mount and fixed to an optical table for testing. The stiffness of each contact and the device as a whole is orders of magnitude larger than the tissue stiffness, such that any error measured is attributed to movement of the mouse and not the device.

PRELIMINARY TESTING OF RESTRAINT DEVICE

This chapter discusses the testing of the restraint device. Section 7.1 outlines the procedure used for testing, and Section 7.2 discusses the predicted performance of the device based on measured material properties for the mouse. Section 7.3 presents the results of preliminary testing.

7.1 Performance Characterization Procedure

To determine the performance a mouse was placed in the restraint device and the force at each location adjusted to a maximum determined by the biological researcher in order to avoid damage to the skull. Then, the displacement of the mouse's skull in each axis was measured.

7.1.1 Testing Procedure

In order to measure the performance of the device, an additional fixture to hold the capacitive probes used for displacement measurement was built. Then, the following protocol was carried out:

- 1) Anesthetize the mouse and remove the skin from the top of the head
- 2) Fix a plastic block with conductive metal coating (copper tape) to the top of the skull with dental cement.
- 3) Place the mouse in the restraint device, and place the anesthetic line in the nose cone.

- 4) Adjust each contact such that it is in the correct location
- 5) Measure force at each contact location using pressure film. Photograph pressure film for later analysis of force.
- 6) Set up the capacitive probe holder such that each probe is within 125 μ m of the block fixed to the mouse skull.
- 7) Record displacement readings for one minute.
- 8) Remove back of head contact and repeat steps 6-7.
- 9) Remove anesthetic and allow mouse to wake up. Record displacement readings after anesthetic stopped.
- 10) Euthanize the mouse
- 11) Remove skin and muscle tissue from contact areas. Perform Instron testing on samples to determine thickness and modulus coefficient.
- 12) Using the measured values for the skin thickness and modulus along with the recorded displacement in each axis, predict the performance of the device using the theory developed in Chapter 5 and compare to actual performance.

7.1.2 Experimental Setup

This procedure was used to characterize the device performance on a single C57BL/6 mouse at the MGH Center for Systems Biology. The testing was approved by MGH's Committee on Animal Care. The restraint device and capacitive probe holder block used to measure the performance are shown in Figure 7.1:

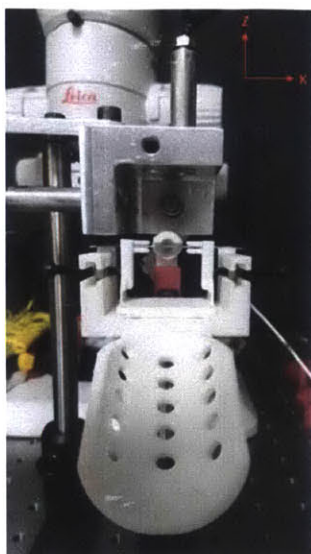


Figure 7.1: Rear view of experimental setup with capacitive probes positioned around location of mouse skull.

The skin was removed from the top of the mouse's skull and the mouse was anesthetized and placed in the holder. Then each of the contacts was hand tightened by a scientist who works with mice on a daily basis. The force at each contact was measured using a pressure film. A cube coated in copper was glued to the mouse's skull to enable displacement readings of the skull position with capacitive probes.

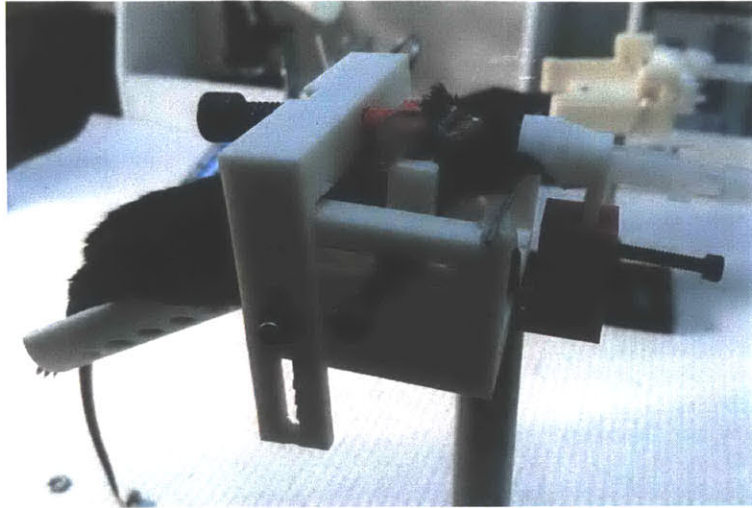


FIG 7.2: Mouse tightened in holder, after removal of skin and before attachment of conductive head block

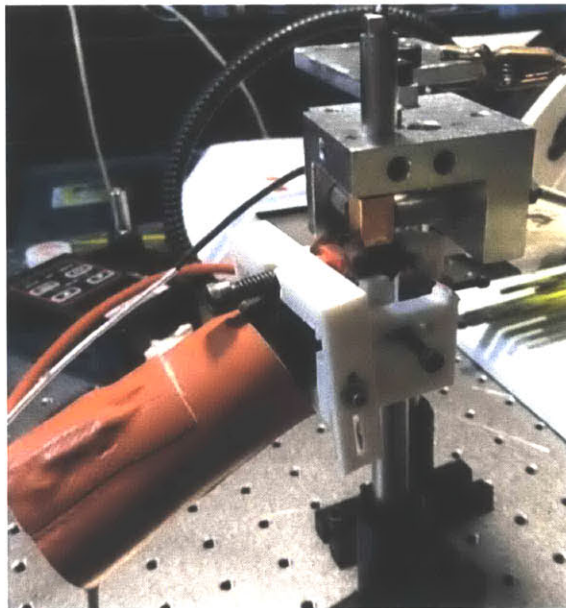


Figure 7.3: Mouse with copper head block in holder. Measurements being taken in each axis with capacitive probes reading the block's displacement over time. The anesthetized mouse is kept at the correct body temperature by the orange body warmer.

7.2 Results

7.2.1 Material Properties

The measured values for thickness, and modulus coefficient, for the locations where tissue samples could be obtained are summarized in Table 17. The muscle layer on the back of the skull was so thin it could not be harvested.

Table 17: Material Property Values for Mouse used in Performance Characterization

Location	q Value	Thickness (μm)	Error (%)
Skin (cheek)	10.2	420	5
Skin (back of head)	11.3	320	4
Muscle (cheek)	9.0	1200	8

7.2.2 Predicted Performance

The tissue properties and force values necessary to predict performance for the restraint of an awake mouse were able to be collected only for the x axis. Then, Equation 34 was used to calculate the predicted worst case displacement in the x axis, using the value calculated for F_M in Section 2.5 and the measured contact force.

$$\delta_x = \frac{t_0}{q} \ln \left(\frac{F_M}{F_A + F_T} + 1 \right) = \frac{1}{4.56} \ln \left(\frac{1.96}{2.01} + 1 \right) = 149 \mu\text{m}$$

For an anesthetized mouse the expected movement is much smaller, although the exact value can not be predicted because the force due to respiration is unknown.

7.2.3 Actual Performance

Capacitive probes measured displacement of the conductive block fixed to the mouse skull at a rate of 1000Hz. The noise was filtered using a moving average filter, as shown in Figure 7.4;

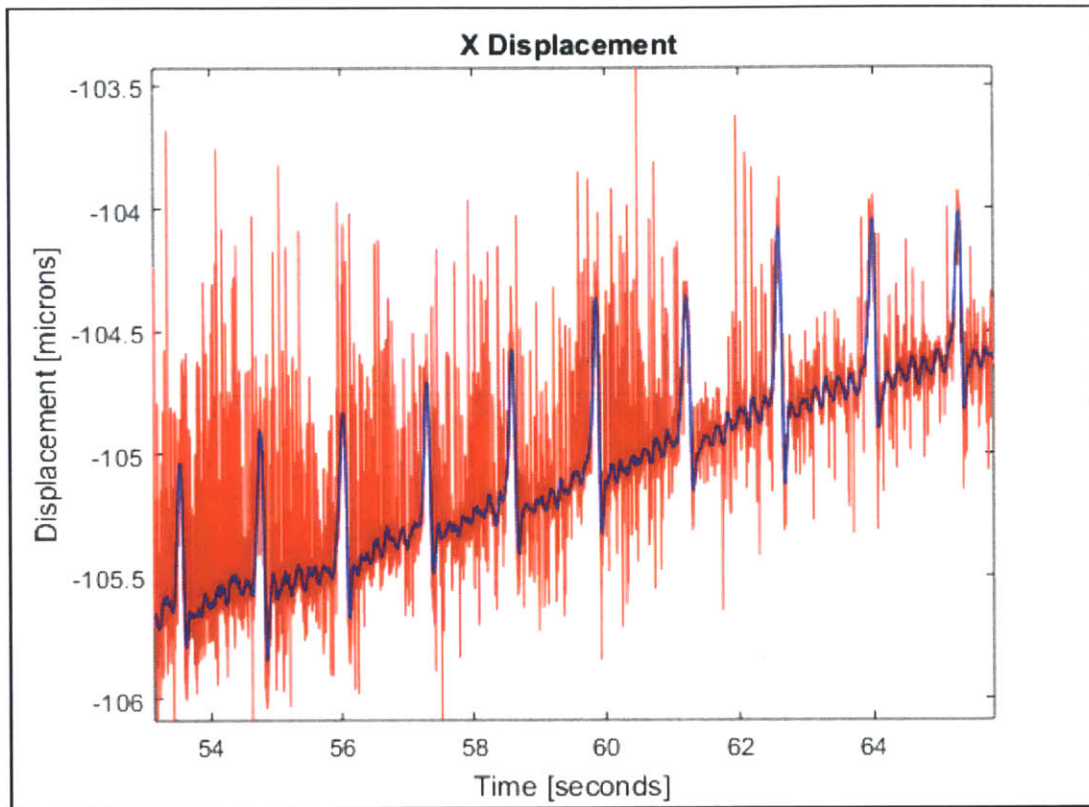


FIG 7.4: Raw data for x displacement shown in red, filtered data (sample size 101) in blue

The displacement due to the heartbeat and respiration is clearly visible, and highlighted in Figure 7.5. The average magnitude of displacement for each axis is summarized in Table 18. These values were calculated by averaging the displacement for five sets of three subsequent breaths or heartbeats spaced five seconds apart in each trial. The uncertainty is equal to the standard deviation plus the error of the capacitive probes, which is $\pm 0.04\mu\text{m}$.

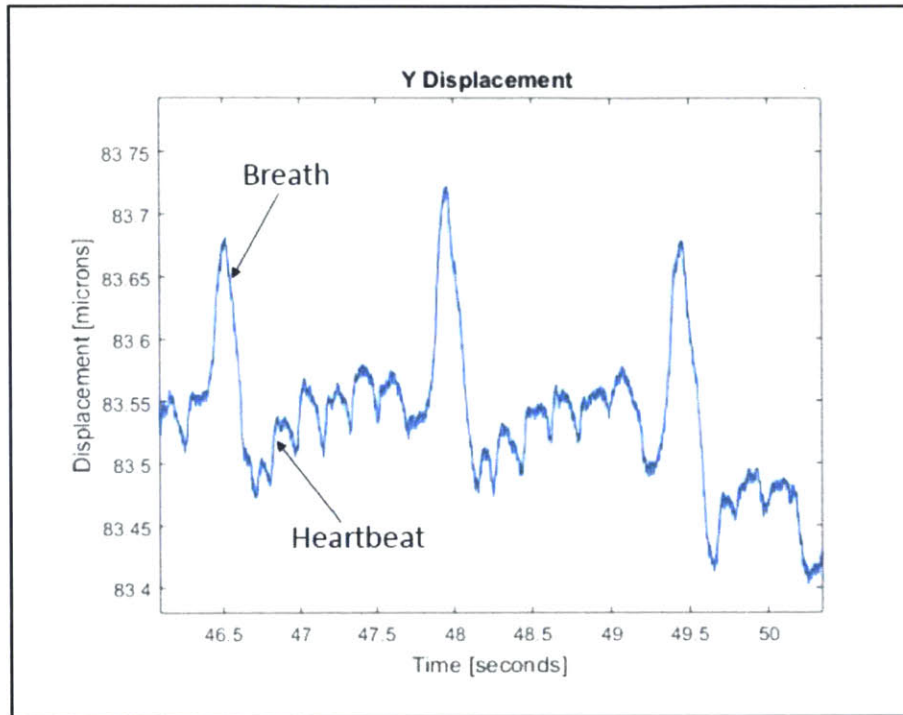


Fig 7.5: Close up view of *y* displacement with back of the head contact used. Breaths occur approximately every second, while heart beats are much more frequent.

To determine the effect of the rear contact on *y* displacement, it was removed and the displacement measured. The average magnitude of displacement in the *y* axis increased without the rear contact from $0.60\mu\text{m}$ to $1.89\mu\text{m}$, shown by Figure 7.6. However, more testing is needed to confirm this trend.

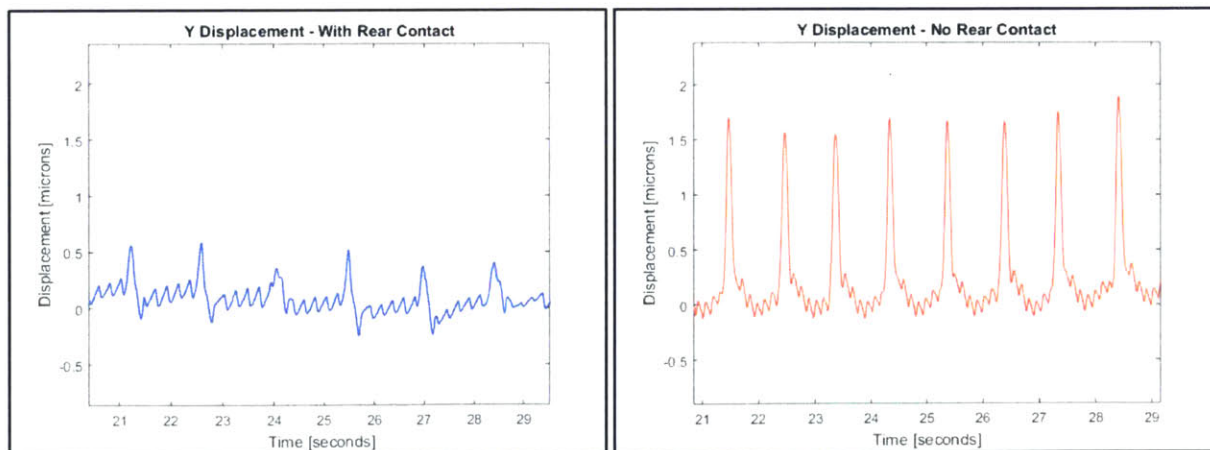


FIGURE 7.6: *y* displacement of skull with (a) and without (b) rear contact

Table 18: Measured Displacement of Anesthetized Mouse Skull in Restraint Device

Axis	Heartbeat [μm]	Uncertainty [μm]	Respiration [μm]	Uncertainty [μm]	Rear Contact?
X	0.10	0.06	0.61	0.13	Yes
X	0.08	0.05	0.60	0.12	No
Y	0.12	0.06	0.60	0.13	Yes
Y	0.30	0.09	1.89	0.32	No
Z	0.05	0.05	0.22	0.08	Yes

To study the efficacy of the device in restraining awake mice, the anesthesia line was removed, and the mouse allowed to wake up. Awakeness was tested using a foot pinch, a common test to determine whether the mouse has come out from anesthesia and can feel pain, an awake mouse will twitch in response to the pinch. The mouse's attempts to escape the restraint device are shown in Figure 7.7.

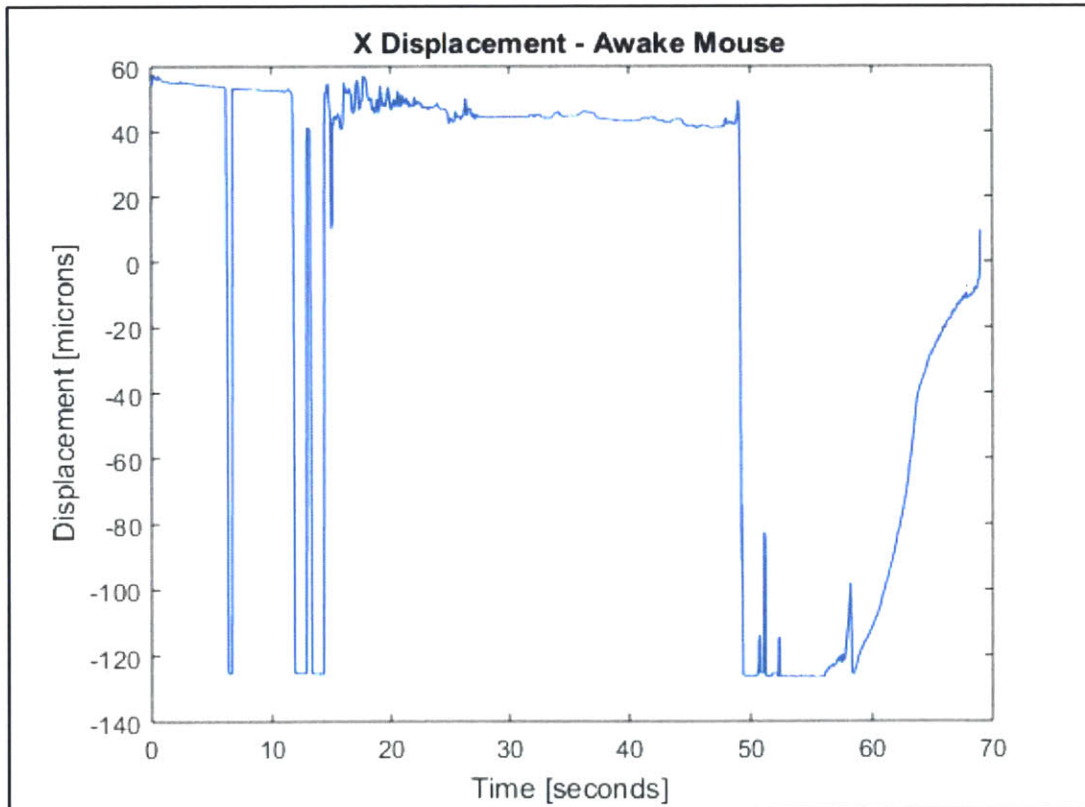


FIG 7.7: Displacement in the x axis for an awake mouse. The range of the capacitive probes ($\pm 125\mu\text{m}$) was surpassed, shown by the flat line at $-125\mu\text{m}$.

The mouse's attempts to escape resulted in displacements greater than 185 μm . This is of the order of magnitude predicted by the theoretical model, demonstrating that this approach is insufficient for constraining animals who are awake and attempting to escape. Figure 7.7 shows that when the animal is not actively attempting to escape the restraint device (time period from 27 – 48 seconds), the restraint device performs sufficiently for images to be captured with the needed resolution. However, as the behavior of the mouse is unpredictable, this is not a viable option.

7.3 Discussion

The average displacement of the anesthetized mouse's skull in the z axis was 0.05 μm for heartbeat and 0.22 μm for respiration. In the x axis, values of 0.10 μm for heartbeat and 0.61 μm for respiration were recorded, while the y axis saw values of 0.12 μm for heartbeat and 0.60 μm for respiration.

Compared to the performance of the initial prototype (Chapter 1.3.2), which limited displacement in the z axis due to heartbeat to an average of 0.02 μm and respiration to 0.1-0.2 μm , the restraint device designed in this thesis performed similarly. The displacement of the initial prototype in the x and y axes was not measured, so no comparison can be drawn there. However, in testing the performance of the device with and without the rear contact, a significant improvement (from 1.89 μm to 0.60 μm) was seen in the y axis when the rear contact was used. This suggests that adding this rear contact would improve the quality of images captured for anesthetized mice. The magnitude of the displacement in other axes was unaffected by the presence of the rear contact.

The ability of the restraint device to constrain an awake mouse was insufficient for the desired application. The theoretical model predicted an x axis displacement of 149 μm , and a

displacement of $\geq 185\mu\text{m}$ was measured. Error sources that may have contributed to the discrepancy include the error in tissue stiffness measurement, error in contact force measurement ($\pm 1\text{N}$), error in the mouse force estimation (unknown), and movement of the capacitive probe holder with respect to the device due to thermal expansion. A more rigorously designed test setup is necessary to eliminate these sources of error, but the agreement in displacement order of magnitude suggests that the theoretical model is a sufficient approximation for the displacement.

The performance of the restraint device will now be compared to the functional requirements outlined in Section 6.1:

Table 19: Restraint Device Functional Requirements Revisited

Metric	Required	Achieved	Units
Slow Drift over 2hrs	0.007	3	$\mu\text{m}/\text{min}$
Mouse Movement (x, y)	<1	0.6	μm
Mouse Movement (z)	<0.7	0.22	μm
Geometry	<5x5	8x8	cm
Applied Force Accuracy	+/- 1	-	N

The designed restraint device met the functional requirements for mouse movement, but further work is needed to meet each of the other requirements. The large slow drift measured could be a result of several factors including thermal expansion of the capacitive probe holder, human activity in the surrounding lab, and creep in the ABS. To improve this, the device should be constructed entirely from aluminum to minimize creep, and tested in the microscope environment where outside factors such as temperature fluctuations and human activity are minimized. Further work to minimize size and include force limiters or sensors with immediate sensors would address the applied force accuracy requirement.

CONCLUSIONS AND FUTURE WORK

8.1 Thesis Synopsis

The purpose of this work was the development of a model to understand the relationship between a constraint system's inputs and its ability to limit the movement of nonlinear elastic objects. The specific objectives of this thesis were to characterize the material properties of mouse tissue, quantify the performance of a constraint system based on input parameters, use the measured tissue properties to predict the performance of a mouse restraint device, and finally build and test such a device.

The direct application of this work was to understand the feasibility of building a mouse skull restraint device capable of limiting the skull to sub-micron movement in each axis for the case of awake and anesthetized mice. This work applied the developed model to the interface between a mouse skull and a rigid contact, simplified the model for the specific application to mouse restraint based on the results of material testing, and determined the relationship between system inputs and performance. This model determined that a constraint system that interfaces with the skin would allow an awake mouse to move hundreds of microns in each axis, demonstrating its inability to achieve the desired sub-micron movement of the awake mouse skull. For the case of the anesthetized mouse, the constraint method achieved sub-micron movement in all three axes, and suggested that a contact on the back of the head is necessary to bring displacement in the y axis to the desired sub-micron magnitude.

8.2 Future Work

8.2.1 Validation of Theoretical Model

To improve and validate the theoretical model for constraint system performance, further testing should be done with more predictable and controllable subjects than laboratory mice. A setup using material with more consistent and easily measurable thickness and modulus properties, such as stock tissue phantoms, and with highly accurate force sensors would decrease the error in the results. This testing would experimentally validate the use of the model as a tool for characterizing the ability of a system to restrict movement of a rigid body surrounded by a nonlinear elastic material.

8.2.2 Improvements to Restraint Device

There are several areas for future work in the improvement of the restraint device. Pending CAC approval, the device should be tested with awake animals in order to determine an experimental value for the mouse force, which would inform future designs. Second, its design can be optimized for the researcher's use by changing the adjustment of each contact to be one handed, and redesigning the back bar support piece such that it does not sit above the imaging plane, enabling the device to reliably fit under a microscope setup. The device design may also be changed to allow for further adjustability in each dimension, enabling use with a wider range of mouse sizes. A force limiting mechanism could also be added to each contact, allowing the researcher to tighten the contacts to the maximum allowable force without fear of causing damage to the mouse.

8.2.3 Application of Theory to Human Restraint for Medical Imaging

The theory developed in this thesis may be applicable to the design of constraint systems for other applications, including human imaging. Currently thermoplastic masks are the most common restraint mechanism for humans, but movement on the order of centimeters may still be seen due to respiration and muscle twitching. Further research must be done to understand the specific challenges of restraining humans before determining whether or not the approach developed here may be applied.

REFERENCES

- [1] Y. Wang, K. L. Marshall, Y. Baba, E. A. Lumpkin, and G. J. Gerling, “Compressive Viscoelasticity of Freshly Excised Mouse Skin Is Dependent on Specimen Thickness, Strain Level and Rate,” *PLoS One*, vol. 10, no. 3, p. e0120897, 2015.
- [2] D. P. Holschneider and J.-M. I. Maarek, “Brain maps on the go: functional imaging during motor challenge in animals.,” *Methods*, vol. 45, no. 4, pp. 255–61, Aug. 2008.
- [3] S. Goel, A. H. Wong, and R. K. Jain, “Vascular Normalization as a Therapeutic Strategy,” *Cold Spring Harb Perspect Med*, vol. 2, pp. 1–24, 2012.
- [4] C. Alt, L. J. Mortensen, and P. Charles, “Characterization of multiphoton microscopy in the bone marrow following intravital laser osteotomy,” vol. 5, no. 10, pp. 3578–3588, 2014.
- [5] A. Mizrahi, J. C. Crowley, E. Shtoyerman, and L. C. Katz, “High-resolution in vivo imaging of hippocampal dendrites and spines.,” *J. Neurosci.*, vol. 24, no. 13, pp. 3147–3151, 2004.
- [6] J. Schallek, Y. Geng, H. Nguyen, and D. R. Williams, “Morphology and topography of retinal pericytes in the living mouse retina using in vivo adaptive optics imaging and ex vivo characterization.,” *Invest. Ophthalmol. Vis. Sci.*, vol. 54, pp. 8237–8250, 2013.
- [7] C. Halin, J. Rodrigo Mora, C. Sumen, and U. H. von Andrian, “in Vivo Imaging of Lymphocyte Trafficking,” *Annu. Rev. Cell Dev. Biol.*, vol. 21, no. 1, pp. 581–603, 2005.
- [8] D. A. Dombeck, A. N. Khabbaz, F. Collman, T. L. Adelman, and D. W. Tank, “Neurotechnique Imaging Large-Scale Neural Activity with Cellular Resolution in Awake , Mobile Mice,” pp. 43–57, 2007.
- [9] R. P. J. Barretto, T. H. Ko, J. C. Jung, T. J. Wang, G. Capps, A. C. Waters, Y. Ziv, A. Attardo, L. Recht, and M. J. Schnitzer, “Time-lapse imaging of disease progression in deep brain areas using fluorescence microendoscopy.,” *Nat. Med.*, vol. 17, no. 2, pp. 223–8, Mar. 2011.
- [10] H. Mizuma, M. Shukuri, T. Hayashi, Y. Watanabe, and H. Onoe, “Establishment of in vivo brain imaging method in conscious mice.,” *J. Nucl. Med.*, vol. 51, no. 7, pp. 1068–75, Jul. 2010.

- [11] L. Herfst, A. Burgalossi, K. Haskic, J. J. Tukker, M. Schmidt, and M. Brecht, "Friction-based stabilization of juxtacellular recordings in freely moving rats," *J. Neurophysiol.*, vol. 108, no. 2, pp. 697–707, 2012.
- [12] K. Shah, "Imaging Neural Stem Cell Fate in Mouse Model of Glioma," 2009.
- [13] M. Culpepper and S.-C. Chen, "NIH_SBIR_draft." pp. 1–4, 2012.
- [14] "Mouse Facts," 12/08/2015. [Online]. Available: http://www.informatics.jax.org/mgihome/other/mouse_facts1.shtml.
- [15] I. T. Nakayama A1, Ogiso B, Tanabe N, Takeichi O, Matsuzaka K, "Behaviour of bone marrow osteoblast-like cells on mineral trioxide aggregate: morphology and expression of type I collagen and bone-related protein mRNAs," *Int. J. Endod.*, vol. 38, no. 4, pp. 203–10, 2005.
- [16] "Medicon Surgical." [Online]. Available: <http://www.medicon.de/index.php?id=2987927&L=1>. [Accessed: 16-Jan-2016].
- [17] H. G. Vogel, "Strain of Rat Skin at Constant Load (Creep Experiments) Influence of Age and Desmotropic Agents," *Gerontology*, vol. 23, no. 2, pp. 77–86, 1977.
- [18] "Skulls Unlimited." [Online]. Available: http://www.skullsunlimited.com/record_variant.php?id=3821. [Accessed: 16-Jan-2016].
- [19] NT-MDT, "The Hertz problem solution," 2016. [Online]. Available: <http://www.ntmdt.com/spm-basics/view/hertz-problem-solution>. [Accessed: 16-Jan-2016].
- [20] Y. Wang, K. L. Marshall, Y. Baba, G. J. Gerling, and E. a Lumpkin, "Hyperelastic Material Properties of Mouse Skin under Compression.," *PLoS One*, vol. 8, no. 6, p. e67439, Jan. 2013.
- [21] B. C. W. Kot, Z. J. Zhang, A. W. C. Lee, V. Y. F. Leung, and S. N. Fu, "Elastic modulus of muscle and tendon with shear wave ultrasound elastography: variations with different technical settings.," *PLoS One*, vol. 7, no. 8, p. e44348, 2012.
- [22] E. J. Chen, J. Novakofski, W. K. Jenkins, and W. D. O. Brien, "with Application to Elasticity Imaging," *Most*, vol. 43, no. 1, pp. 191–194, 1996.
- [23] R. Kruse, C. Weichert, and M. Bol, "Elastic Properties of Muscle Tissue: Comparison of an Inverse Finite Element Approach and Homogeneous Deformation," *Proceeding Appl. Math. Mech.*, vol. 12, pp. 101–102, 2012.
- [24] I. Kasza, Y. Suh, D. Wollny, R. J. Clark, A. Roopra, R. J. Colman, O. A. MacDougald, T.

- A. Shedd, D. W. Nelson, M.-I. Yen, C.-L. E. Yen, and C. M. Alexander, "Syndecan-1 is required to maintain intradermal fat and prevent cold stress.," *PLoS Genet.*, vol. 10, no. 8, p. e1004514, 2014.
- [25] H. Mao, C. Wagner, F. Guan, Y. N. Yeni, and K. H. Yang, "Material Properties of Adult Rat Skull," *J. Mech. Med. Biol.*, vol. 11, no. 05, pp. 1199–1212, Dec. 2011.
- [26] A. Ledberg and D. Robbe, "Locomotion-Related Oscillatory Body Movements at 6–12 Hz Modulate the Hippocampal Theta Rhythm," *PLoS One*, vol. 6, no. 11, p. e27575, 2011.
- [27] S. Venkatraman, J. D. Long, K. S. J. Pister, J. M. Carmena, and A. Hardware, "Wireless Inertial Sensors for Monitoring Animal Behavior," *Proc. 29th Annu. Int. Conf. IEEE EMBS*, pp. 378–381, 2007.
- [28] M. S. Fee and M. Hill, "Active Stabilization of Electrodes for Intracellular Recording in Awake Behaving Animals," vol. 27, pp. 461–468, 2000.
- [29] A. H. Slocum, *Precision Machine Design*. Society of Manufacturing Engineers, 1992.

ELECTRONICS SCHEMATIC

A.1 VCA Control

The PCB schematic for the voice coil actuator op amp is shown in Figure A.1. The power resistor R_{sense} was grounded to a large heatsink.

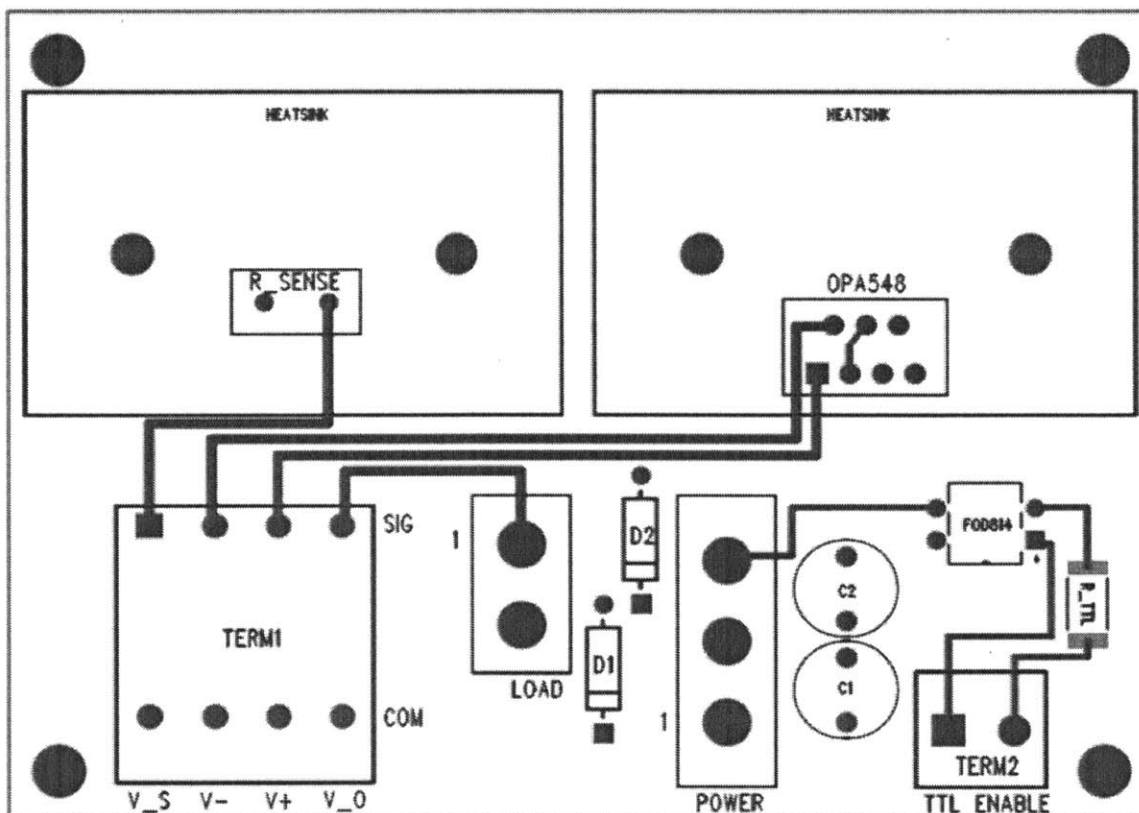


Figure A.1: PCB Layout for VCA Control Op Amp